Inverse scattering for Schrödinger equation in the frequency domain via data-driven reduced order modeling [*]

Andreas Tataris[†], Tristan van Leeuwen[‡], and Alexander V. Mamonov[§]

Abstract. In this paper we develop a numerical method for solving an inverse scattering problem of estimating the scattering potential in a Schrödinger equation from frequency domain measurements based on reduced order models (ROM). The ROM is a projection of Schrödinger operator onto a subspace spanned by its solution snapshots at certain wavenumbers. Provided the measurements are performed at these wavenumbers, the ROM can be constructed in a data-driven manner from the measurements on a surface surrounding the scatterers. Once the ROM is computed, the scattering potential can be estimated using non-linear optimization that minimizes the ROM misfit. Such an approach typically outperforms the conventional methods based on data misfit minimization. We develop two variants of ROM-based algorithms for inverse scattering and test them on a synthetic example in two spatial dimensions.

Key words. Inverse scattering, full waveform inversion, frequency domain, model order reduction.

MSC codes. 65M32, 41A20

1. Introduction. Inverse scattering problems are ubiquitous in the areas of science and engineering where one wants to reconstruct either non-penetrable scatterers or to examine material properties of media without direct physical access to it. In this paper we focus on an inverse scattering problem that belongs to the latter type, of estimating the scattering potential of a Schrödinger operator in two or more dimensions. Such inverse problem can be treated in the unbounded case using elegant analytical tools leading to the Gelfand-Levitan and Marchenko equation [9]. However, in this paper we approach the solution of the inverse problem by combining nonlinear optimization with the techniques originating from the so-called reduced order models.

Reduced order models (ROM) have been used extensively in numerical analysis of PDEs as alternative to conventional solution methods due to their fast convergence properties and cmomputational efficiency, e.g., see [18, 25]. In particular, projection ROMs are used to compute approximate solutions of PDEs as expansions in the bases of solutions to the same PDE corresponding to various values of the scalar parameter of the problem, e.g., time or wavenumber. In addition, over the last several years data-driven projection ROMs were employed to construct efficient numerical methods for solving a variety of inverse problems. These studies include inversion for coefficients of diffusive PDEs from frequency-domain measurements, e.g., see [1, 2, 13, 14], as well as estimating coefficients of wave PDEs from time-domain data

---

[†]Delft University of Technology, The Netherlands (A.Tataris@tudelft.nl).

[‡]Utrecht University and CWI Amsterdam, The Netherlands (t.vanleeuwen@uu.nl).

[§]Department of Mathematics, University of Houston, Houston, TX, USA (avmamonov@uh.edu).

[3, 4, 5, 6, 7, 11, 12, 19]. For a while a question stood as to whether data-driven ROM-based approaches are applicable to wave PDEs in the frequency domain. Recently, this question was resolved positively in [23, 24], where data-driven ROM techniques were successfully applied to the numerical solution of a classical inverse scattering problem in one spatial dimension as an alternative to the conventional Gelfand-Levitan-Marchenko point of view. In this work we extend this approach to solve numerically an inverse scattering problem for the scattering potential of Schrödinger equation in two or more spatial dimensions in a bounded domain from the knowledge of frequency-domain measurements on the boundary of the domain of interest.

Most of the ROM-based approaches to solving inverse problems discussed above share a similar structure. Typically, such inversion procedures consist of two stages. In the first stage one computes from the measured data a ROM of the PDE operator, hence the designation data-driven. The ROM is a projection of the PDE operator with the unknown coefficient on a subspace spanned by the solutions of the PDE for a number of values of the scalar parameter, time of wavenumber depending on the measurement setting. Even though the projection involves an unknown PDE operator and the solutions in the bulk that are also unknown, certain algebraic techniques as well as the properties of PDE operators make it possible to compute such projections from the knowledge of the data only, typically measured on or near the boundary of the domain of interest. In the second stage one needs to extract the information about the PDE coefficient of interest from the data-driven ROM computed in the first stage. One option is to use nonlinear optimization to minimize the least squares misfit between the data-driven ROM and the reduced model computed for a trial coefficient of the PDE. While each iteration of such optimization is as expensive as minimizing the least squares data misfit, a conventional approach to solving inverse problems, minimizing ROM misfit is almost always superior to data misfit minimization. In particular, for wave problems ROM misfit optimization objective is much better behaved (close to convex) than data misfit objective, as shown in extensive numerical studies in [5, 7]. Thus, ROM-based optimization converges much faster and is less prone to getting stuck in local minima, which leads also to decreased sensitivity to the initial guess and ultimately to higher quality estimates of the PDE coefficient.

We follow here the outline for ROM-based inversion described above. First, from the knowledge of boundary data we reconstruct the Galerkin projection of the continuous Schrödinger operator onto the space spanned by the solutions of the Schrödinger equation corresponding to several wave numbers. This is made possible by the formulas for data-driven computation of mass and stiffness matrices for the Schrödinger equation in Galerkin framework. Next, the unknown Schrödinger coefficient is estimated by solving a nonlinear optimization problem that minimizes the ROM misfit. We explore two possible formulations, that are the two main contributions in this work. One minimizes the stiffness matrix misfit directly as in [24], while the other transforms the stiffness matrix to a block-tridiagonal form using block-Lanczos process prior to minimization, as motivated by [1, 2, 23].

The paper is organized as follows. We begin in Section 2 by setting up the forward problem, as well as data model and the particular formulation of the inverse scattering problem. We also introduce projection ROM of the kind that is computable in a data-driven way. Section 3 contains the main theoretical results as well as numerical algorithms for computing the ROM

from the data, transforming ROM matrices to block tridiagonal form and setting the nonlinear optimization problem of minimizing ROM misfit to estimate the scattering potential. We continue in Section 4 presenting the details of implementation of the proposed approach and the results of numerical experiments in two spatial dimensions. We conclude in Section 5 with a brief discussion of the results and directions for future research.

2. Preliminaries and problem formulation.

2.1. Forward model.
In classical inverse scattering one considers the Schrödinger equation

$$(2.1) \qquad \left[-\Delta + q(\mathbf{x}) - k^2\right] u(\mathbf{x}; k) = 0, \quad \mathbf{x} = [x_1, \dots, x_d] \in \mathbb{R}^d,$$

in the whole space $\mathbb{R}^d$ for $d = 2, 3$. The total wavefield is decomposed into an incoming wave $u^{\mathrm{inc}}(\mathbf{x}; k)$ and scattered wave $u^{\mathrm{scat}}(\mathbf{x}; k)$ so that

$$(2.2) \qquad u(\mathbf{x}; k) = u^{\mathrm{inc}}(\mathbf{x}; k) + u^{\mathrm{scat}}(\mathbf{x}; k)$$

and the scattered wavefield satisfies a radiation condition at infinity, e.g., Sommerfeld condition

$$(2.3) \qquad \lim_{r \to \infty} r^{\frac{d-1}{2}} \left(\frac{\partial}{\partial r} - \imath k\right) u^{\mathrm{scat}}(\mathbf{x}; k) = 0,$$

where $r = \sqrt{x_1^2 + \dots + x_d^2}$. Here $k \in \mathbb{R}_+$ is the wavenumber and the scattering potential $q(\mathbf{x})$ is the quantity of interest. Typically, it is assumed that the target scatterer has compact support in a bounded domain $\Omega \subset \mathbb{R}^d$, i.e., $\overline{\mathrm{supp}(q)} \subset\subset \Omega$. Then, the target scatterer is illuminated by a number of incident wavefields and the corresponding far-field scattered wavefields are measured. The classical inverse scattering problem is then to recover q from these measurements, see for example [21, 20, 8].

For a more realistic measurement setting we modify the problem (2.1)–(2.3) to work with a finite domain $\Omega \subset \mathbb{R}^d$ instead of the whole $\mathbb{R}^d$. Thus, we pose the Schrödinger equation in Ω only:

$$(2.4) \qquad \left[-\Delta + q(\mathbf{x}) - k^2\right] u^{(s)}(\mathbf{x}; k) = 0, \quad \mathbf{x} \in \Omega,$$

More importantly, we approximate the radiation condition (2.3) with an impedance boundary condition

$$(2.5) \qquad [\mathbf{n}(\mathbf{x}) \cdot \nabla - \imath k] u^{(s)}(\mathbf{x}; k) = p_s(\mathbf{x}), \quad \mathbf{x} \in \partial\Omega,$$

where $\mathbf{n} : \partial\Omega \to \mathbb{R}^d$ is the outward facing normal on $\partial\Omega$ and the dot denotes the standard inner product of vectors in $\mathbb{R}^d$. Right away we point a few differences between the conventional formulation (2.1)–(2.3) and our setting (2.4)–(2.5). First, the total wavefield is no longer decomposed into an incoming and scattered components. This leads to the second difference, the non-zero right-hand side of the boundary condition (2.5). Note that the zero right hand side in (2.5) turns it into the absorbing boundary condition introduced in [15]. In our setting the term

$$(2.6) \qquad p_s \in H^{1/2}(\partial\Omega; \mathbb{R}), \quad s = 1, \dots, m,$$

now plays the role of the source of illumination. We refer to p_s as the sources, and to facilitate illumination of the target scatterer from multiple directions, we employ m of them assuming they satisfy a non-overlapping condition

$$(2.7) \qquad \operatorname{supp}(p_{s_1}) \cap \operatorname{supp}(p_{s_2}) = \varnothing, \text{ for } s_1 \neq s_2.$$

The wavefield solutions of (2.4)–(2.5) corresponding to the excitation by source s are denoted by $u^{(s)}(\mathbf{x}; k)$, $s = 1, \ldots, m$.

Note that we can relate the formulation (2.4)–(2.5) with boundary sources to that with incoming waves by choosing

$$(2.8) \qquad p_s(\mathbf{x}) = \xi^{(s)}(\mathbf{x}) \left[\mathbf{n}(\mathbf{x}) \cdot \nabla - \imath k\right] u^{\mathrm{inc},(s)}(\mathbf{x}; k), \quad \mathbf{x} \in \partial\Omega, \quad s = 1, \ldots, m,$$

where we select m incoming waves $u^{\mathrm{inc},(s)}(\mathbf{x}; k)$ in such way that the right-hand side of (2.8) does not depend on the wavenumber k. The factors $\xi^{(s)}(\mathbf{x})$ are the indicator functions of $\operatorname{supp}(p_s)$ chosen to satisfy (2.7). Physically, they represent windows through which the incoming wave passes before illuminating the domain of interest Ω.

Assuming that the target scatterer satisfies $q \in L^\infty_+(\Omega) := L^\infty(\Omega; (0, \infty))$, the forward problem (2.4)–(2.5) admits a weak (variational) formulation

$$(2.9) \qquad \int_\Omega \overline{\nabla u^{(s)}} \cdot \nabla v \, d\mathbf{x} + \int_\Omega q\overline{u^{(s)}}v d\mathbf{x} - k^2 \int_\Omega \overline{u^{(s)}}v d\mathbf{x} + \imath k \int_{\partial\Omega} \overline{u^{(s)}}v d\Sigma = \int_{\partial\Omega} \overline{p_s}v d\Sigma,$$

for all $v \in H^1(\Omega)$ and $s = 1, \ldots, m$. The existence and uniqueness of solutions of (2.9) is guaranteed by the following result.

Theorem 2.1. *Given $k \in \mathbb{R}_+ := (0, \infty)$, $q \in L^\infty_+(\Omega)$ with $\overline{supp(q)} \subset\subset \Omega$, and boundary source $p_s \in H^{1/2}(\partial\Omega)$, the problem (2.9) admits the unique weak solution $u^{(s)}(\,\cdot\,; k) \in H^1(\Omega)$.*

The proof is similar to that for the Helmholtz case [26, 23]. For a sketch of the proof we refer to Appendix C. Later, we will assume that the source functions admit real values.

2.2. Operator form and Fréchet differentiation. In this section we introduce the operator formulation of the forward model. Its use is twofold. First, the ROM framework developed in this work relies on finite-dimensional projections of the operators entering this formulation, as explained in Section 2.4. Second, the operator formulation helps in deriving the Fréchet derivative of the solution wavefield with respect to the wave number k. These derivatives are required for computing the ROM from the measurements.

We begin by defining the three operators

$$(2.10) \qquad \mathcal{S}, \mathcal{M}, \mathcal{B} : H^1(\Omega) \to H^1(\Omega)'.$$

Let $\langle \cdot, \cdot \rangle_{H^1(\Omega)'}$ be the pairing between $H^1(\Omega)$ and the corresponding space of distributions $H^1(\Omega)'$. Then, for all $f, g \in H^1(\Omega)$ we define $\mathcal{S}, \mathcal{M}$ and $\mathcal{B}$ by

$$(2.11) \qquad \langle \mathcal{S}f, g \rangle_{H^1(\Omega)'} = \int_\Omega \overline{\nabla f} \cdot \nabla g \, d\mathbf{x} + \int_\Omega q \overline{f} g \, d\mathbf{x},$$

$$(2.12) \qquad \langle \mathcal{M}f, g \rangle_{H^1(\Omega)'} = \int_\Omega \overline{f} g \, d\mathbf{x},$$

$$(2.13) \qquad \langle \mathcal{B}f, g \rangle_{H^1(\Omega)'} = \int_{\partial\Omega} \overline{f} g \, d\Sigma.$$

Next, we introduce

$$(2.14) \qquad F^{(s)} : (k, u) \in \mathbb{R}_+ \times H^1(\Omega) \to H^1(\Omega)', \quad s = 1, \dots, m,$$

as

$$(2.15) \qquad F^{(s)}(k, u) = (\mathcal{S} - k^2 \mathcal{M} + \imath k \mathcal{B})u - P^{(s)}, \quad (k, u) \in \mathbb{R}_+ \times H^1(\Omega), \quad s = 1, \dots, m,$$

where $P^{(s)} \in H^1(\Omega)'$ is defined by

$$\left\langle P^{(s)}, g \right\rangle_{H^1(\Omega)'} = \int_{\partial\Omega} \overline{p_s} g \, d\Sigma = \int_{\partial\Omega} p_s g \, d\Sigma$$

for any $g \in H^1(\Omega)$, assuming that $p_s \in H^{1/2}(\partial\Omega; \mathbb{R}), \ s = 1, ..., m$.

Remark 2.2. The weak problem (2.9) can be expressed in the operator form using (2.11)–(2.15) as a problem of finding $u^{(s)}(\cdot; k) \in H^1(\Omega)$ satisfying

$$(2.16) \qquad (\mathcal{S} - k^2 \mathcal{M} + \imath k \mathcal{B})u^{(s)}(\cdot; k) = P^{(s)}, \quad s = 1, \dots, m.$$

Operator formulation (2.16) allows to differentiate the solution $u^{(s)}(\mathbf{x}; k)$ in Fréchet sense with respect to the wavenumber k by applying the implicit function theorem to $F^{(s)}$. The following result establishes the boundary value problem satisfied by Fréchet derivative.

Theorem 2.3. *Let $q \in L^\infty_+(\Omega)$. The wavefields $u^{(s)}(\mathbf{x}; k)$ satisfying (2.4)–(2.5) are differentiable with respect to k and their Fréchet derivatives at $k = k_0$ denoted by $\partial_k u^{(s)}(\mathbf{x}; k_0) = w^{(s)}(\mathbf{x})$, are weak solutions of the following problem*

$$(2.17) \qquad \left[-\Delta + q(\mathbf{x}) - k_0^2 \right] w^{(s)}(\mathbf{x}) = 2k_0 u^{(s)}(\mathbf{x}; k_0), \quad \mathbf{x} \in \Omega, \quad s = 1, \dots, m,$$

with boundary condition

$$(2.18) \qquad \left[\mathbf{n}(\mathbf{x}) \cdot \nabla - \imath k_0 \right] w^{(s)}(\mathbf{x}) = \imath u^{(s)}(\mathbf{x}; k_0), \quad \mathbf{x} \in \partial\Omega, \quad s = 1, \dots, m.$$

The proof based on the implicit function theorem is given in Appendix B.

2.3. Measurements and the inverse scattering problem. In practice, performing measurements of the solutions of (2.9) at all wavenumbers $k \in \mathbb{R}_+$ is infeasible. Thus, the first assumption we make about the measurement setup is that we only have access to information about the wavefields at a finite number n of distinct sampling wavenumbers

$$(2.19) \qquad 0 < k_1 < k_2 < \ldots < k_n.$$

We use these wavenumbers to define the *snapshots* of wavefields and their derivatives

$$(2.20) \qquad u_j^{(s)}(\mathbf{x}) = u^{(s)}(\mathbf{x}; k_j), \quad \partial_k u_j^{(s)}(\mathbf{x}) = \partial_k u^{(s)}(\mathbf{x}; k_j), \quad j = 1, \ldots, n, \quad s = 1, \ldots, m,$$

Note that in inverse scattering one does not have access to the snapshots, but only to their "far field" measurements, which in our setting correspond to boundary traces that we denote by

$$(2.21) \qquad \phi_j^{(s)} = u_j^{(s)}\Big|_{\partial\Omega}, \quad \partial_k \phi_j^{(s)} = \partial_k u_j^{(s)}\Big|_{\partial\Omega}, \quad j = 1, \ldots, n, \quad s = 1, \ldots, m.$$

Thus, we assume that the data has the form

$$(2.22) \qquad \mathcal{D} = \left\{ \phi_j^{(s)}, \partial_k \phi_j^{(s)} \right\}_{j=1,\ldots,n; s=1,\ldots,m}.$$

Practically, the trace derivative data $\partial_k \phi_j^{(s)}$ can be obtained by measuring boundary traces $u^{(s)}(\mathbf{x}; k)\big|_{\partial\Omega}$ at one or more wavenumbers close to k_j followed by interpolation and numerical differentiation. We can now formulate the inverse scattering problem that we address here.

Inverse scattering problem (ISP). Given the data (2.22) estimate the scattering potential $q \in L_+^\infty(\Omega)$.

Remark 2.4. We use the term "estimate" in the formulation of the ISP above since in general it may be impossible to recover exactly the scattering potential q from the finite amount of data in (2.22).

Remark 2.5. As we shall see in what follows, the pointwise knowledge of the traces (2.22) on $\partial\Omega$ is not needed for the construction of the ROMs of the kind that we intend to use. Instead, the knowledge of certain integrals involving the traces in $\mathcal{D}$ is sufficient. However, to keep the formulation of the ISP concise and clear, we assume that the whole of $\mathcal{D}$ can be measured.

2.4. Projection reduced order model. At the heart of the approach proposed here for the numerical solution of the ISP formulated above are the techniques of projection-based model order reduction. The first step in all such approaches [19, 2, 13] is to project the operators (2.10) onto the reduced order space

$$(2.23) \qquad \mathcal{X} = \text{span} \left\{ u_j^{(s)} \right\}_{j=1,\ldots,n; \ s=1,\ldots,m}$$

spanned by the wavefield snapshots (2.20). If the snapshots for all sampling wavenumbers and all sources are linearly independent, then

$$(2.24) \qquad \dim(\mathcal{X}) = mn.$$

While eventually we are interested in orthogonal projections of (2.10) onto $\mathcal{X}$, we postpone this discussion until Section 3.1.2. For now, we consider the stiffness and mass matrices along with another boundary matrix that arise if we view the problem (2.16) in Galerkin framework. Specifically, we introduce the matrices

$$(2.25) \qquad \mathbf{S}, \mathbf{M}, \mathbf{B} \in \mathbb{C}^{mn \times mn},$$

referred to as the stiffness, mass and boundary matrices. Hereafter we denote $mn \times mn$ matrices by bold uppercase letters. Due to the indexing of snapshots according to sampling wavenumbers and source numbers, all three matrices (2.25) have a block structure consisting of $n \times n$ blocks of size $m \times m$ each, e.g.,

$$(2.26) \qquad \mathbf{S} = \begin{bmatrix} \mathbf{s}_{11} & \mathbf{s}_{12} & \dots & \mathbf{s}_{1n} \\ \mathbf{s}_{21} & \mathbf{s}_{22} & \dots & \mathbf{s}_{2n} \\ \vdots & \vdots & \ddots & \vdots \\ \mathbf{s}_{n1} & \mathbf{s}_{n2} & \dots & \mathbf{s}_{nn} \end{bmatrix} \in \mathbb{C}^{mn \times mn},$$

with

$$(2.27) \qquad \mathbf{s}_{ij} \in \mathbb{C}^{m \times m}, \quad i,j = 1, \dots, n.$$

Likewise,

$$(2.28) \qquad \mathbf{M} = [\mathbf{m}_{ij}]_{i,j=1,\dots,n}, \quad \mathbf{m}_{ij} \in \mathbb{C}^{m \times m}, \quad i,j = 1, \dots, n,$$

$$(2.29) \qquad \mathbf{B} = [\mathbf{b}_{ij}]_{i,j=1,\dots,n}, \quad \mathbf{b}_{ij} \in \mathbb{C}^{m \times m}, \quad i,j = 1, \dots, n.$$

We refer to the sub-matrices $\mathbf{s}_{ij}$, $\mathbf{m}_{ij}$ and $\mathbf{b}_{ij}$ in (2.26)–(2.29) as the blocks and hereafter denote them by bold lowercase letters.

Following the standard Galerkin framework, we use the formulas (2.11)–(2.13) that define the operators (2.10) to express the blocks of the three matrices (2.25) in terms of their individual entries

$$(2.30) \qquad [\mathbf{s}_{ij}]_{rs} = \left\langle \mathcal{S}u_i^{(r)}, u_j^{(s)} \right\rangle_{H^1(\Omega)'} = \int_\Omega \overline{\nabla u_i^{(r)}} \cdot \nabla u_j^{(s)} d\mathbf{x} + \int_\Omega q \overline{u_i^{(r)}} u_j^{(s)} d\mathbf{x},$$

$$(2.31) \qquad [\mathbf{m}_{ij}]_{rs} = \left\langle \mathcal{M}u_i^{(r)}, u_j^{(s)} \right\rangle_{H^1(\Omega)'} = \int_\Omega \overline{u_i^{(r)}} u_j^{(s)} d\mathbf{x},$$

$$(2.32) \qquad [\mathbf{b}_{ij}]_{rs} = \left\langle \mathcal{B}u_i^{(r)}, u_j^{(s)} \right\rangle_{H^1(\Omega)'} = \int_{\partial\Omega} \overline{u_i^{(r)}} u_j^{(s)} d\Sigma,$$

where the block indices run over wavenumber indices $i,j = 1, \dots, n$, while the entries within each block are indexed by the "source/receiver" indices $r,s = 1, \dots, m$. Clearly, the formulas (2.30)–(2.32) imply that the blocks of the stiffness, mass and boundary matrices for all $i,j = 1, \dots, n$, and $r,s = 1, \dots, m$, satisfy

$$(2.33) \qquad [\mathbf{s}_{ij}]_{rs} = \overline{[\mathbf{s}_{ji}]}_{sr},$$

$$(2.34) \qquad [\mathbf{m}_{ij}]_{rs} = \overline{[\mathbf{m}_{ji}]}_{sr},$$

$$(2.35) \qquad [\mathbf{b}_{ij}]_{rs} = \overline{[\mathbf{b}_{ji}]}_{sr},$$

or simply

$$(2.36) \qquad \mathbf{s}_{ij} = \mathbf{s}_{ji}^*, \quad \mathbf{m}_{ij} = \mathbf{m}_{ji}^*, \quad \mathbf{b}_{ij} = \mathbf{b}_{ji}^*, \quad i,j = 1,\ldots,n,$$

which means that the three corresponding matrices are Hermitian

$$(2.37) \qquad \mathbf{S} = \mathbf{S}^*, \quad \mathbf{M} = \mathbf{M}^*, \quad \mathbf{B} = \mathbf{B}^*.$$

In addition, (2.37) in conjunction with (2.31) and (2.24) also implies that $\mathbf{M}$ is positive-definite.

Note that in order to compute the blocks of $\mathbf{S}$ and $\mathbf{M}$ using relations (2.30)–(2.31) one requires the knowledge of the wavefield snapshots in the whole Ω, while we are interested in solving the ISP where we only have access to the traces (2.22). Incidentally, the mass and stiffness matrices possess a remarkable property that allows their blocks to be computed from the data $\mathcal{D}$ only. Since the matrices $\mathbf{S}$, $\mathbf{M}$ and $\mathbf{B}$ can be thought of as the ROM of the operators $\mathcal{S}$, $\mathcal{M}$ and $\mathcal{B}$, respectively, we will therefore refer to such ROM as data-driven. Computing the ROM in the data-driven manner is discussed in detail in the next section.

3. Main results and the method. In this section we introduce the method for the numerical solution of the ISP based on data-driven ROM. First, we study the computation of the ROM matrices (2.25) from the data (2.22). Next, we consider orthogonal projection ROM obtained by means of the block Lanczos algorithm. Once the ROM is computed, we formulate the optimization problem for solving the ISP via regularized ROM misfit minimization.

3.1. Data-driven ROM. As mentioned in Section 2.4 even though the ROM matrices (2.25) are defined in terms of the wavefield snapshots in the bulk of Ω, it is possible to compute them in a data-driven way making them useful for solving the ISP numerically. Assuming we have access to snapshot traces in $\mathcal{D}$, we can compute the following integral quantities. First, we need the blocks

$$(3.1) \qquad \mathbf{d}_j, \partial_k \mathbf{d}_j \in \mathbb{C}^{m \times m}, \quad j = 1,\ldots,n,$$

defined entrywise as

$$(3.2) \qquad [\mathbf{d}_j]_{rs} = \int_{\partial\Omega} \overline{p_r} u_j^{(s)} d\Sigma = \int_{\partial\Omega} p_r u_j^{(s)} d\Sigma,$$

$$(3.3) \qquad [\partial_k \mathbf{d}_j]_{rs} = \int_{\partial\Omega} \overline{p_r} \partial_k u_j^{(s)} d\Sigma = \int_{\partial\Omega} p_r \partial_k u_j^{(s)} d\Sigma,$$

with $r,s = 1,\ldots,m$ and $j = 1,\ldots,n$, where we used assumption (2.6) that the sources are real valued. This allows us to obtain the following reciprocity result.

Proposition 3.1. *The blocks* (3.2) *are complex-symmetric*

$$(3.4) \qquad \mathbf{d}_j^T = \mathbf{d}_j, \quad j = 1,\ldots,n.$$

Proof. For a fixed $j \in \{1, 2, \ldots, n\}$ we begin by taking the complex conjugate of (2.9):

$$(3.5) \qquad \int_\Omega \nabla u_j^{(s)} \cdot \overline{\nabla v} \, d\mathbf{x} + \int_\Omega q u_j^{(s)} \overline{v} d\mathbf{x} - k_j^2 \int_\Omega u_j^{(s)} \overline{v} d\mathbf{x} - \imath k_j \int_{\partial\Omega} u_j^{(s)} \overline{v} d\Sigma = \int_{\partial\Omega} p_s \overline{v} d\Sigma,$$

then, choosing $v = \overline{u_j^{(r)}}$, we obtain

(3.6)
$$\int_\Omega \nabla u_j^{(s)} \cdot \nabla u_j^{(r)} \, d\mathbf{x} + \int_\Omega q u_j^{(s)} u_j^{(r)} d\mathbf{x} - k_j^2 \int_\Omega u_j^{(s)} u_j^{(r)} d\mathbf{x} - \imath k_j \int_{\partial\Omega} u_j^{(s)} u_j^{(r)} d\Sigma = \int_{\partial\Omega} p_s u_j^{(r)} d\Sigma.$$

On the other hand, replacing s with r in (3.5) and taking the test function to be $v = \overline{u_j^{(s)}}$, we arrive at

(3.7)
$$\int_\Omega \nabla u_j^{(r)} \cdot \nabla u_j^{(s)} \, d\mathbf{x} + \int_\Omega q u_j^{(r)} u_j^{(s)} d\mathbf{x} - k_j^2 \int_\Omega u_j^{(r)} u_j^{(s)} d\mathbf{x} - \imath k_j \int_{\partial\Omega} u_j^{(r)} u_j^{(s)} d\Sigma = \int_{\partial\Omega} p_r u_j^{(s)} d\Sigma.$$

Since the left-hand sides of (3.6) and (3.7) are equal, the same holds for the right-hand sides

$$(3.8) \qquad [\mathbf{d}_j]_{sr} = \int_{\partial\Omega} p_s u_j^{(r)} d\Sigma = \int_{\partial\Omega} p_r u_j^{(s)} d\Sigma = [\mathbf{d}_j]_{rs}, \quad s, r = 1, \ldots, m,$$

which immediately implies (3.4). ∎

Note that since

$$(3.9) \qquad [\partial_k \mathbf{d}_j]_{rs} = \int_{\partial\Omega} p_r \partial_k u_j^{(s)} d\Sigma = \partial_k \left[\int_{\partial\Omega} p_r(\mathbf{x}) u^{(s)}(\mathbf{x}; k) d\Sigma(\mathbf{x}) \right] \Big|_{k=k_j},$$

it follows from (3.2) and (3.4) that the derivative blocks (3.3) are complex-symmetric as well

$$(3.10) \qquad [\partial_k \mathbf{d}_j]^T = \partial_k \mathbf{d}_j, \quad j = 1, \ldots, n.$$

We also need the boundary matrix and blocks

$$(3.11) \qquad \mathbf{B} \in \mathbb{C}^{mn \times mn}, \quad \mathbf{c}_j \in \mathbb{C}^{m \times m}, \quad j = 1, \ldots, n,$$

defined as

$$(3.12) \qquad [\mathbf{b}_{ij}]_{rs} = \int_{\partial\Omega} \overline{u_i^{(r)}} u_j^{(s)} d\Sigma,$$

$$(3.13) \qquad [\mathbf{c}_j]_{rs} = \int_{\partial\Omega} \left[-\overline{u_j^{(r)}} \partial_k u_j^{(s)} + u_j^{(s)} \overline{\partial_k u_j^{(r)}} \right] d\Sigma,$$

with $i, j = 1, \ldots, n$, and $r, s = 1, \ldots, m$. As established already in Section 2.4, the blocks (3.12) are Hermitian and so is $\mathbf{B}$. It follows directly from the definition (3.13) that the boundary blocks $\mathbf{c}_j$ are skew-Hermitian

$$(3.14) \qquad \mathbf{c}_j^* = -\mathbf{c}_j, \quad j = 1, \ldots, n.$$

As explained later, the stiffness and mass matrices, $\mathbf{S}$ and $\mathbf{M}$, respectively, are completely determined by the boundary integral quantities (3.2)–(3.3) and (3.12)–(3.13). Thus, the knowledge of the whole data set $\mathcal{D}$ is not needed for our approach to solving the ISP. Instead, the knowledge of

$$(3.15) \qquad\qquad \{\mathbf{B}, \mathbf{c}_j, \mathbf{d}_j, \partial_k \mathbf{d}_j\}_{j=1,\ldots,n}$$

is sufficient. However, for the sake of simplicity we stick to the ISP formulation from Section 2.3 since the data $\mathcal{D}$ can be easily converted to the knowledge of (3.15) using (3.2)–(3.3) and (3.12)–(3.13).

3.1.1. Data-driven stiffness and mass matrix computaion.
We provide here the formulas for computing the blocks (2.30)–(2.31) of the stiffness and mass matrices from (3.15) and thus from the data (2.22). Note that the formulas for the off-diagonal and diagonal blocks are different, hence we formulate them as separate propositions below. The proofs of all the propositions that follow can be found in Appendix A.

Proposition 3.2. *The off-diagonal blocks $\mathbf{s}_{ij} \in \mathbb{C}^{m \times m}$, $i, j = 1, \ldots, n$, $i \neq j$, of the stiffness matrix (2.30) are given by*

$$(3.16) \qquad\qquad \mathbf{s}_{ij} = \frac{k_i^2 \mathbf{d}_i^* - k_j^2 \mathbf{d}_j}{k_i^2 - k_j^2} - \imath \frac{(k_i k_j^2 + k_i^2 k_j)\mathbf{b}_{ij}}{k_i^2 - k_j^2}.$$

Proposition 3.3. *The diagonal blocks $\mathbf{s}_{jj} \in \mathbb{C}^{m \times m}$, $j = 1, \ldots, n$, of the stiffness matrix (2.30) are given by*

$$(3.17) \qquad\qquad \mathbf{s}_{jj} = \frac{1}{2}\left(k_j \Re(\partial_k \mathbf{d}_j) + 2\Re(\mathbf{d}_j)\right) + \frac{\imath k_j^2}{2} \mathbf{c}_j.$$

Proposition 3.4. *The off-diagonal blocks $\mathbf{m}_{ij} \in \mathbb{C}^{m \times m}$, $i, j = 1, \ldots, n$, $i \neq j$, of the mass matrix (2.31) are given by*

$$(3.18) \qquad\qquad \mathbf{m}_{ij} = \frac{\mathbf{d}_i^* - \mathbf{d}_j}{k_i^2 - k_j^2} - \imath \frac{\mathbf{b}_{ij}}{k_j - k_i}.$$

Proposition 3.5. *The diagonal blocks $\mathbf{m}_{jj} \in \mathbb{C}^{m \times m}$, $j = 1, \ldots, n$, of the mass matrix (2.31) are given by*

$$(3.19) \qquad\qquad \mathbf{m}_{jj} = \frac{1}{2k_j} \Re(\partial_k \mathbf{d}_j) + \frac{\imath}{2} \mathbf{c}_j.$$

We summarize data-driven stiffness and mass matrix computation in Algorithm 3.1 below.

3.1.2. Orthogonal projection ROM via block-Lanczos algorithm.
In view of relation (2.30), we observe that the dependence of the stiffness matrix $\mathbf{S}$ on the potential of interest q is affine provided the snapshots are known. This dependence is approximately affine if the snapshots depend weakly on q. If neither is the case, one may wish to transform the ROM matrix $\mathbf{S}$ further so that it corresponds to an orthogonal projection of $\mathcal{S}$ onto the reduced

---

Algorithm 3.1 Data-driven stiffness and mass matrix computation

Input: boundary data $\mathcal{D} = \left\{ \phi_j^{(s)}, \partial_k \phi_j^{(s)} \right\}_{j=1,\ldots,n;s=1,\ldots,m}$.

• Compute the blocks

$$(3.20) \qquad [\mathbf{b}_{ij}]_{rs} = \int_{\partial\Omega} \overline{\phi_i^{(r)}} \phi_j^{(s)} d\Sigma,$$

$$(3.21) \qquad [\mathbf{c}_j]_{rs} = \int_{\partial\Omega} \left[-\overline{\phi_j^{(r)}} \partial_k \phi_j^{(s)} + \phi_j^{(s)} \overline{\partial_k \phi_j^{(r)}} \right] d\Sigma,$$

$$(3.22) \qquad [\mathbf{d}_j]_{rs} = \int_{\partial\Omega} p_r \phi_j^{(s)} d\Sigma,$$

$$(3.23) \qquad [\partial_k \mathbf{d}_j]_{rs} = \int_{\partial\Omega} p_r \partial_k \phi_j^{(s)} d\Sigma,$$

for $i, j = 1, \ldots, n$, $r, s = 1, \ldots, m$.
• Compute the blocks $\mathbf{s}_{ij} \in \mathbb{C}^{m \times m}$ and $\mathbf{m}_{ij}$, $i, j = 1, \ldots, n$, using formulas (3.16)–(3.19).
Output: mass and stiffness matrices $\mathbf{M}$ and $\mathbf{S}$.

---

order space (2.23). This requires introduction of the so-called orthogonalized snapshots $v_j^{(s)}$ that form an orthonormal basis for the reduced space $\mathcal{X}$:

$$(3.24) \qquad \mathcal{X} = \mathrm{span} \left\{ v_j^{(s)} \right\}_{j=1,\ldots,n; \ s=1,\ldots,m},$$

where orthonormality is understood as

$$(3.25) \qquad \int_\Omega \overline{v_i^{(r)}} v_j^{(s)} d\mathbf{x} = \delta_{ij} \delta_{rs}, \quad i, j = 1, \ldots, n, \quad r, s = 1, \ldots, m.$$

We are interested in a specific orthonormal basis so that the projection of $\mathcal{S}$ onto $\mathcal{X}$ in this basis has the block-tridiagonal form

$$(3.26) \qquad \mathbf{T} = \begin{bmatrix} \boldsymbol{\alpha}_1 & \boldsymbol{\beta}_2 & \mathbf{0} & \ldots & \mathbf{0} \\ \boldsymbol{\beta}_2^* & \boldsymbol{\alpha}_2 & \boldsymbol{\beta}_3 & \ddots & \vdots \\ \mathbf{0} & \boldsymbol{\beta}_3^* & \ddots & \ddots & \mathbf{0} \\ \vdots & \ddots & \ddots & \boldsymbol{\alpha}_{n-1} & \boldsymbol{\beta}_n \\ \mathbf{0} & \ldots & \mathbf{0} & \boldsymbol{\beta}_n^* & \boldsymbol{\alpha}_n \end{bmatrix} \in \mathbb{C}^{mn \times mn},$$

with blocks $\boldsymbol{\alpha}_i, \boldsymbol{\beta}_j \in \mathbb{C}^{m \times m}$ given entrywise by

$$(3.27) \quad [\boldsymbol{\alpha}_i]_{rs} = \left\langle \mathcal{S} v_i^{(r)}, v_i^{(s)} \right\rangle_{H^1(\Omega)'} = \int_\Omega \overline{\nabla v_i^{(r)}} \cdot \nabla v_i^{(s)} d\mathbf{x} + \int_\Omega q \overline{v_i^{(r)}} v_i^{(s)} d\mathbf{x}, \qquad i = 1, \ldots, n,$$

$$(3.28) \quad [\boldsymbol{\beta}_j]_{rs} = \left\langle \mathcal{S} v_{j-1}^{(r)}, v_j^{(s)} \right\rangle_{H^1(\Omega)'} = \int_\Omega \overline{\nabla v_{j-1}^{(r)}} \cdot \nabla v_j^{(s)} d\mathbf{x} + \int_\Omega q \overline{v_{j-1}^{(r)}} v_j^{(s)} d\mathbf{x}, \quad j = 2, \ldots, n.$$

Such a basis can be computed by applying the block-Lanczos process to the matrix

$$(3.29) \qquad \widetilde{\mathbf{S}} = \mathbf{M}^{-1/2}\mathbf{S}\mathbf{M}^{-1/2} \in \mathbb{C}^{mn \times mn}$$

and the starting column-block

$$(3.30) \qquad \widetilde{\mathbf{d}} = \mathbf{M}^{1/2} \begin{bmatrix} \overline{\mathbf{d}_1} \\ \overline{\mathbf{d}_2} \\ \vdots \\ \overline{\mathbf{d}_n} \end{bmatrix} \in \mathbb{C}^{mn \times m}.$$

Note that since $\mathbf{M}$ is positive-definite, as mentioned in Section 2.4, there exists a unique positive-definite matrix square root $\mathbf{M}^{1/2} \in \mathbb{C}^{mn \times mn}$. The presence of the terms $\mathbf{M}^{-1/2}$ and $\mathbf{M}^{1/2}$ in (3.29) and (3.30), respectively, enables the use of the regular block-Lanczos process based on the standard $\mathbb{C}^{mn}$-inner product. Alternatively, one may apply block-Lanczos directly to $\mathbf{S}$ and the starting column-block $[\mathbf{d}_1, \mathbf{d}_2, \ldots, \mathbf{d}_n]^*$, but then a modification is needed for all inner products in block-Lanczos process to be computed in $\mathbf{M}$-weighted inner product. In any case, the resulting matrix $\mathbf{T}$ is the same, so we opt for a simpler variant of block-Lanczos as discussed below.

The block-Lanczos process given in Algorithm 3.2 computes a block-tridagonal matrix $\mathbf{T}$ and a unitary matrix $\mathbf{Q} \in \mathbb{C}^{mn \times mn}$ that can be written in block-column form

$$(3.31) \qquad \mathbf{Q} = [\mathbf{q}_1, \mathbf{q}_2, \ldots, \mathbf{q}_n], \quad \mathbf{q}_j \in \mathbb{C}^{mn \times m}, \quad j = 1, \ldots, n,$$

satisfying

$$(3.32) \qquad \mathbf{q}_i^* \mathbf{q}_j = \delta_{ij} \mathbf{I}_m \in \mathbb{C}^{m \times m}, \quad i, j = 1, \ldots, n,$$

where $\mathbf{I}_m$ is the $m \times m$ identity matrix. The matrix $\mathbf{Q}$ defines a unitary change of coordinates such that

$$(3.33) \qquad \mathbf{T} = \mathbf{Q}^* \widetilde{\mathbf{S}} \mathbf{Q} = \mathbf{Q}^* \mathbf{M}^{-1/2} \mathbf{S} \mathbf{M}^{-1/2} \mathbf{Q}.$$

Algorithm 3.2 contains an optional reorthogonalization step for increased numerical stability. In practice, the computational cost of this step is negligible compared to the overall cost of solving the ISP using the transformed ROM matrix $\mathbf{T}$. Therefore, we perform reorthogonalization at every step of Algorithm 3.2.

Relation (3.33) implies an explicit formula for the orthogonalized snapshots. Introducing notation

$$(3.34) \quad \mathbf{u}_j(\mathbf{x}) = \left[u_j^{(1)}(\mathbf{x}), u_j^{(2)}(\mathbf{x}), \ldots, u_j^{(m)}(\mathbf{x}) \right], \quad \mathbf{v}_j(\mathbf{x}) = \left[v_j^{(1)}(\mathbf{x}), v_j^{(2)}(\mathbf{x}), \ldots, v_j^{(m)}(\mathbf{x}) \right],$$

with $\mathbf{u}_j, \mathbf{v}_j : \Omega \to \mathbb{C}^{1 \times m}$, $j = 1, \ldots, n$, we can express the orthogonalized snapshots as

$$(3.35) \qquad [\mathbf{v}_1(\mathbf{x}), \ldots, \mathbf{v}_n(\mathbf{x})] = [\mathbf{u}_1(\mathbf{x}), \ldots, \mathbf{u}_n(\mathbf{x})] \, \mathbf{M}^{-1/2} \mathbf{Q}, \quad \mathbf{x} \in \Omega.$$

Observe that (2.31) can be written as

$$(3.36) \qquad \int_\Omega \mathbf{u}_i^*(\mathbf{x})\mathbf{u}_j(\mathbf{x})d\mathbf{x} = \mathbf{m}_{ij}, \quad i,j = 1,\ldots,n,$$

which in conjunction with (3.32) implies

$$(3.37) \qquad \int_\Omega \mathbf{v}_i^*(\mathbf{x})\mathbf{v}_j(\mathbf{x})d\mathbf{x} = \delta_{ij}\mathbf{I}_m, \quad i,j = 1,\ldots,n,$$

which is a matrix form of orthogonality relations (3.25).

Algorithm 3.2 Block Lanczos Process

Input: matrix $\widetilde{\mathbf{S}} \in \mathbb{C}^{mn \times mn}$ and starting block-column $\widetilde{\mathbf{d}} \in \mathbb{C}^{mn \times m}$.

- Set $\boldsymbol{\beta}_1 = \left(\widetilde{\mathbf{d}}^*\widetilde{\mathbf{d}}\right)^{1/2}$;
- Set $\mathbf{q}_1 = \widetilde{\mathbf{d}}\,\boldsymbol{\beta}_1^{-1}$;
- Set $\mathbf{w} = \widetilde{\mathbf{S}}\mathbf{q}_1$;

for $j = 1,\ldots,n-1$ **do**
    1. Set $\boldsymbol{\alpha}_j = \mathbf{w}^*\mathbf{q}_j$;
    2. Update $\mathbf{w} = \mathbf{w} - \mathbf{q}_j\boldsymbol{\alpha}_j$;
    3. If needed, perform reorthogonalization by updating

$$\mathbf{w} = \mathbf{w} - [\mathbf{q}_1,\ldots,\mathbf{q}_j]\left([\mathbf{q}_1,\ldots,\mathbf{q}_j]^*\mathbf{w}\right);$$

    4. Set $\boldsymbol{\beta}_{j+1} = (\mathbf{w}^*\mathbf{w})^{1/2}$;
    5. Set $\mathbf{q}_{j+1} = \mathbf{w}\,\boldsymbol{\beta}_{j+1}^{-1}$;
    6. Set $\mathbf{w} = \widetilde{\mathbf{S}}\mathbf{q}_{j+1} - \mathbf{q}_j\boldsymbol{\beta}_{j+1}$;
end for
- Set $\boldsymbol{\alpha}_n = \mathbf{w}^*\mathbf{q}_n$;

Output: the blocks $\boldsymbol{\alpha}_j, \boldsymbol{\beta}_j \in \mathbb{C}^{m \times m}$, $j = 1,\ldots,n$, of $\mathbf{T}$ and the unitary matrix $\mathbf{Q} = [\mathbf{q}_1,\ldots,\mathbf{q}_n] \in \mathbb{C}^{mn \times mn}$.

We conclude this section with Algorithm 3.3 for computing the block-tridiagonal matrix $\mathbf{T}$ in a data-driven manner.

Algorithm 3.3 Data-driven block tridiagonal matrix computation

---

Input: boundary data $\mathcal{D} = \left\{\phi_j^{(s)}, \partial_k\phi_j^{(s)}\right\}_{j=1,\ldots,n;s=1,\ldots,m}$.

- Use Algorithm 3.1 to compute $\mathbf{S} \in \mathbb{C}^{mn \times mn}$ and $\mathbf{M} \in \mathbb{C}^{mn \times mn}$ from $\mathcal{D}$.
- Form $\widetilde{\mathbf{S}} \in \mathbb{C}^{mn \times mn}$ and $\widetilde{\mathbf{d}} \in \mathbb{C}^{mn \times m}$ using (3.29) and (3.30), respectively.
- Apply Algorithm 3.2 to $\widetilde{\mathbf{S}}$ and $\widetilde{\mathbf{d}}$ to compute $\mathbf{T} \in \mathbb{C}^{mn \times mn}$.

Output: block-tridiagonal $\mathbf{T} \in \mathbb{C}^{mn \times mn}$.

3.2. Numerical solution of ISP via ROM misfit minimization. Conventionally, one may solve the ISP numerically in the following manner. Consider the mapping from the potential q to the boundary data $\mathcal{D}$ defined by expressions (2.4)–(2.5), (2.17)–(2.18), (2.20)–(2.22) and denoted by

$$(3.38) \qquad \mathcal{D}[q] = \left\{ \phi_j^{(s)}[q], \partial_k \phi_j^{(s)}[q] \right\}_{j=1,\dots,n;s=1,\dots,m}.$$

Then, a typical approach to numerical solution of the ISP is via non-linear least squares

$$(3.39) \qquad \underset{\widehat{q} \in \mathcal{Q}}{\text{minimize}} \sum_{j=1}^{n} \sum_{s=1}^{m} \int_{\partial \Omega} \left| \phi_j^{(s)} - \phi_j^{(s)}[\widehat{q}] \right|^2 d\Sigma,$$

where $\phi_j^{(s)}$ is the measured data, $\widehat{q}$ is the search potential and $\mathcal{Q}$ is some a priori chosen search space, typically finite-dimensional.

The formulation (3.39) is known to have its limitations including possibly slow convergence and lack of robustness with respect to the initial guess due to non-convexity of the objective, see for example [17, 22] and the references therein. On the other hand, extensive studies of using data-driven ROMs for estimating the coefficients of wave equations in time domain suggest that reformulating (3.39) as a ROM misfit minimization often leads to objective convexification consequently improving convergence and robustness. Thus, we propose two possible ROM-based approaches to the numerical solution of the ISP. Both approaches have the form

$$(3.40) \qquad \underset{\widehat{q} \in \mathcal{Q}}{\text{minimize}} \, \mathcal{F}(\widehat{q}) + \mu \mathcal{R}(\widehat{q}),$$

where $\mathcal{F}(\widehat{q})$ is the ROM misfit functional, $\mathcal{R}(\widehat{q})$ is the regularization functional and $\mu > 0$ is the regularization parameter. The two possible choices of ROM misfit functionals are

$$(3.41) \qquad \mathcal{F}_{\mathbf{S}}(\widehat{q}) = \left\| \text{Triu}(\mathbf{S}^{\text{meas}} - \mathbf{S}[\widehat{q}]) \right\|_2^2$$

and

$$(3.42) \qquad \mathcal{F}_{\mathbf{T}}(\widehat{q}) = \left\| \text{Triu}(\mathbf{T}^{\text{meas}} - \mathbf{T}[\widehat{q}]) \right\|_2^2.$$

The notation in (3.42)–(3.41) is as follows. We denote by $\text{Triu} : \mathbb{C}^{mn \times mn} \to \mathbb{C}^{mn(mn+1)/2}$ the operation of taking the entries in the upper triangular part of a matrix and stacking them in a vector. The stiffness and block-tridiagonal matrices $\mathbf{S}^{\text{meas}}$ and $\mathbf{T}^{\text{meas}}$, respectively, are computed from the measured, possibly noisy data $\mathcal{D}^{\text{meas}}$, while their analogues $\mathbf{T}[\widehat{q}]$ and $\mathbf{S}[\widehat{q}]$ are computed from $\mathcal{D}[\widehat{q}]$ corresponding to the search potential $\widehat{q}$.

Before continuing further, we should discuss the effects of noise in the data on solving the ISP using ROMs. We define the noisy measurement data $\mathcal{D}^{\text{meas}}$ similarly to noiseless data (2.22):

$$(3.43) \qquad \mathcal{D}^{\text{meas}} = \left\{ \phi_j^{\text{meas},(s)} = \phi_j^{(s)} + \xi_j^{(s)}, \partial_k \phi_j^{\text{meas},(s)} = \partial_k \phi_j^{(s)} + \chi_j^{(s)} \right\}_{j=1,\dots,n;s=1,\dots,m},$$

with the exception of adding the terms $\xi_j^{(s)}$ and $\chi_j^{(s)}$ that model the noise in the measurements of the wavefield and its derivative with respect to k at the boundary $\partial\Omega$. Note that the effect of noise on constructing $\mathbf{S}^{\mathrm{meas}}$ and $\mathbf{T}^{\mathrm{meas}}$ from (3.43) could be profound. In particular, as discussed in Section 2.4 the mass matrix is Hermitian positive definite, and so is the stiffness matrix provided $q(\mathbf{x}) \geq 0$. This property may be broken if $\mathbf{M}^{\mathrm{meas}}$ and $\mathbf{S}^{\mathrm{meas}}$ are assembled from noisy $\mathcal{D}^{\mathrm{meas}}$ using Algorithm 3.1. Thus, a modification of (3.41)–(3.42) is needed to accommodate the noise in (3.43).

First, consider modifying (3.41) to work with noisy data. One may notice that the spectrum of both $\mathbf{M}^{\mathrm{meas}}$ and $\mathbf{S}^{\mathrm{meas}}$ is not affected by the noise uniformly. Instead, for realistic noise models (e.g., the noise model described in Section 4), the small eigenvalues of $\mathbf{M}^{\mathrm{meas}}$ and $\mathbf{S}^{\mathrm{meas}}$ are more sensitive and thus may cross over into the negative values making the mass and stiffness matrices indefinite. Therefore, one possible approach to modifying (3.41) is via spectral projection. Consider the spectral decomposition of the stiffness matrix

$$(3.44) \qquad \mathbf{S}^{\mathrm{meas}} = \mathbf{Z_S} \mathbf{\Lambda_S} \mathbf{Z_S^*},$$

where $\mathbf{\Lambda_S} = \mathrm{diag}\left(\lambda_1^{\mathbf{S}}, \lambda_2^{\mathbf{S}}, \ldots, \lambda_{mn}^{\mathbf{S}}\right)$ with eigenvalues sorted as $\lambda_1^{\mathbf{S}} \geq \lambda_2^{\mathbf{S}} \geq \ldots \geq \lambda_{mn}^{\mathbf{S}}$, and the columns of $\mathbf{Z_S} \in \mathbb{C}^{mn \times mn}$ are the corresponding eigenvectors of $\mathbf{S}^{\mathrm{meas}}$. Note that due to the presence of noise in $\mathcal{D}^{\mathrm{meas}}$, it is possible for some eigenvalues in (3.44) to be negative. Then, modification of (3.41) is needed when $\lambda_{mn}^{\mathbf{S}} < 0$. In both cases we choose an integer $r_{\mathbf{S}}$ such that

$$(3.45) \qquad r_{\mathbf{S}} = \begin{cases} \max_{\lambda_{mr}^{\mathbf{S}} \geq |\lambda_{mn}^{\mathbf{S}}|} r, & \text{if } \lambda_{mn}^{\mathbf{S}} < 0, \\ n, & \text{otherwise.} \end{cases}$$

This heuristic allows to identify the number of eigenvalues and eigenvectors of $\mathbf{S}^{\mathrm{meas}}$ that are less sensitive to noise. Denote by $\mathbf{Z_S^r} \in \mathbb{C}^{mn \times mr_{\mathbf{S}}}$ the sub-matrix of $\mathbf{Z_S}$ containing its first $mr_{\mathbf{S}}$ columns. Then, the corresponding stable subspace is

$$(3.46) \qquad \mathcal{Z}_{\mathbf{S}}^r = \mathrm{colspan}(\mathbf{Z_S^r}),$$

with the corresponding spectral projector

$$(3.47) \qquad \mathbf{P_S^r} = \mathbf{Z_S^r} \left(\mathbf{Z_S^r}\right)^*.$$

Note that $\mathbf{P_S^n} = \mathbf{I}_{mn}$, i.e., no projection is needed when $r = n$. Once the stable subspace is computed, the modified objective (3.41) becomes

$$(3.48) \qquad \mathcal{F}_{\mathbf{S}}^r(\widehat{q}) = \left\| \mathrm{Triu}\left[\mathbf{P_S^r} \left(\mathbf{S}^{\mathrm{meas}} - \mathbf{S}[\widehat{q}]\right) \mathbf{P_S^r} \right] \right\|_2^2.$$

Second, modifying (3.42) to work with noisy data requires more effort. In this case we begin with the spectral decomposition of the mass matrix

$$(3.49) \qquad \mathbf{M}^{\mathrm{meas}} = \mathbf{Z_M} \mathbf{\Lambda_M} \mathbf{Z_M^*},$$

with $\mathbf{\Lambda_M} = \mathrm{diag}\left(\lambda_1^{\mathbf{M}}, \lambda_2^{\mathbf{M}}, \ldots, \lambda_{mn}^{\mathbf{M}}\right)$ and $\lambda_1^{\mathbf{M}} \geq \lambda_2^{\mathbf{M}} \geq \ldots \geq \lambda_{mn}^{\mathbf{M}}$. Similarly to (3.45), we take

$$(3.50) \qquad r_{\mathbf{M}} = \begin{cases} \max_{\lambda_{mr}^{\mathbf{M}} \geq |\lambda_{mn}^{\mathbf{M}}|} r, & \text{if } \lambda_{mn}^{\mathbf{M}} < 0, \\ n, & \text{otherwise,} \end{cases}$$

and define the stable subspace

$$(3.51) \qquad\qquad \mathcal{Z}_{\mathbf{M}}^r = \mathrm{colspan}(\mathbf{Z}_{\mathbf{M}}^r),$$

where $\mathbf{Z}_{\mathbf{M}}^r \in \mathbb{C}^{mn \times mr_{\mathbf{M}}}$ contains the first $mr_{\mathbf{M}}$ columns of $\mathbf{Z}_{\mathbf{M}}$. Unlike the construction of (3.48), a number of additional steps is required here. In particular, relations (3.29)–(3.30) need to be modified as follows. Denoting

$$(3.52) \qquad\qquad \mathbf{\Lambda}_{\mathbf{M}}^r = \mathrm{diag}\left(\lambda_1^{\mathbf{M}}, \lambda_2^{\mathbf{M}}, \ldots, \lambda_{mr_{\mathbf{M}}}^{\mathbf{M}}\right) \in \mathbb{R}^{mr_{\mathbf{M}} \times mr_{\mathbf{M}}},$$

we introduce

$$(3.53) \qquad\qquad \widetilde{\mathbf{S}}^r = (\mathbf{\Lambda}_{\mathbf{M}}^r)^{-1/2}(\mathbf{Z}_{\mathbf{M}}^r)^* \, \mathbf{S}^{\mathrm{meas}} \, \mathbf{Z}_{\mathbf{M}}^r(\mathbf{\Lambda}_{\mathbf{M}}^r)^{-1/2} \in \mathbb{C}^{mr_{\mathbf{M}} \times mr_{\mathbf{M}}},$$

and

$$(3.54) \qquad\qquad \widetilde{\mathbf{d}}^r = (\mathbf{\Lambda}_{\mathbf{M}}^r)^{1/2}(\mathbf{Z}_{\mathbf{M}}^r)^* \begin{bmatrix} \overline{\mathbf{d}_1}^{\mathrm{meas}} \\ \overline{\mathbf{d}_2}^{\mathrm{meas}} \\ \vdots \\ \overline{\mathbf{d}_n}^{\mathrm{meas}} \end{bmatrix} \in \mathbb{C}^{mr_{\mathbf{M}} \times m},$$

the analogues of (3.29) and (3.30), respectively. Then, to obtain the modified block tridiagonal matrix $\mathbf{T}^r$, an analogue of Algorithm 3.3 can be formulated as Algorithm 3.4 below.

The computation of $\mathbf{T}[\widehat{q}]$ for the search potential $\widehat{q}$ should also be modified accordingly to the construction of $\mathbf{T}^r$, as outlined below. Denote by $\mathbf{M}[\widehat{q}]$ and $\mathbf{S}[\widehat{q}]$ the stiffness and mass matrices corresponding to the search potential $\widehat{q}$. Once the stable subspace is found in Algorithm 3.4, compute the projection

$$(3.55) \qquad\qquad \mathbf{M}^r[\widehat{q}] = (\mathbf{Z}_{\mathbf{M}}^r)^* \, \mathbf{M}[\widehat{q}] \, \mathbf{Z}_{\mathbf{M}}^r,$$

and use it to calculate

$$(3.56) \qquad\qquad \widetilde{\mathbf{S}}^r[\widehat{q}] = (\mathbf{M}^r[\widehat{q}])^{-1/2}(\mathbf{Z}_{\mathbf{M}}^r)^* \, \mathbf{S}[\widehat{q}] \, \mathbf{Z}_{\mathbf{M}}^r(\mathbf{M}^r[\widehat{q}])^{-1/2} \in \mathbb{C}^{mr_{\mathbf{M}} \times mr_{\mathbf{M}}},$$

and

$$(3.57) \qquad\qquad \widetilde{\mathbf{d}}^r[\widehat{q}] = (\mathbf{M}^r[\widehat{q}])^{1/2} \, (\mathbf{Z}_{\mathbf{M}}^r)^* \begin{bmatrix} \overline{\mathbf{d}_1}[\widehat{q}] \\ \overline{\mathbf{d}_2}[\widehat{q}] \\ \vdots \\ \overline{\mathbf{d}_n}[\widehat{q}] \end{bmatrix} \in \mathbb{C}^{mr_{\mathbf{M}} \times m}.$$

Then, Algorithm 3.2 can be applied to $\widetilde{\mathbf{S}}^r[\widehat{q}]$ and $\widetilde{\mathbf{d}}^r[\widehat{q}]$ with $n = r_{\mathbf{M}}$ to compute $\mathbf{T}^r[\widehat{q}] \in \mathbb{C}^{mr_{\mathbf{M}} \times mr_{\mathbf{M}}}$. The modification of (3.42) then takes the form

$$(3.58) \qquad\qquad \mathcal{F}_{\mathbf{T}}^r(\widehat{q}) = \left\|\mathrm{Triu}(\mathbf{T}^r - \mathbf{T}^r[\widehat{q}])\right\|_2^2.$$

Algorithm 3.4 Data-driven block tridiagonal matrix computation from noisy data

Input: noisy data $\mathcal{D}^{\mathrm{meas}}$ as in (3.43).
- Use Algorithm 3.1 to compute $\mathbf{S}^{\mathrm{meas}} \in \mathbb{C}^{mn \times mn}$ and $\mathbf{M}^{\mathrm{meas}} \in \mathbb{C}^{mn \times mn}$ from $\mathcal{D}^{\mathrm{meas}}$.
- Symmetrize the blocks of $\mathbf{M}^{\mathrm{meas}}$ and $\mathbf{S}^{\mathrm{meas}}$ to enforce (2.35) in case those relations were broken by the presence of noise.
- Compute the eigendecomposition (3.49), choose $r_{\mathbf{M}}$ as in (3.52) and form the matrices $\mathbf{Z}_{\mathbf{M}}^r$ and $\mathbf{\Lambda}_{\mathbf{M}}^r$.
- Form $\widetilde{\mathbf{S}}^r \in \mathbb{C}^{mr_{\mathbf{M}} \times mr_{\mathbf{M}}}$ and $\widetilde{\mathbf{d}}^r \in \mathbb{C}^{mr_{\mathbf{M}} \times m}$ using (3.53) and (3.54), respectively.
- Apply Algorithm 3.2 to $\widetilde{\mathbf{S}}^r$ and $\widetilde{\mathbf{d}}^r$ with $n = r_{\mathbf{M}}$ to compute $\mathbf{T}^r \in \mathbb{C}^{mr_{\mathbf{M}} \times mr_{\mathbf{M}}}$.

Output: block-tridiagonal $\mathbf{T}^r \in \mathbb{C}^{mr_{\mathbf{M}} \times mr_{\mathbf{M}}}$ and the basis for the stable subspace contained in $\mathbf{Z}_{\mathbf{M}}^r \in \mathbb{C}^{mn \times mr_{\mathbf{M}}}$.

As mentioned above, we consider a finite-dimensional search space

$$(3.59) \qquad \mathcal{Q} = \mathrm{span}\{\eta_1(\mathbf{x}), \ldots, \eta_N(\mathbf{x})\},$$

with $N < mn(mn+1)/2$, so that the search potential has the form

$$(3.60) \qquad \widehat{q}(\mathbf{x}; \mathbf{y}) = \sum_{l=1}^{N} y_l \eta_l(\mathbf{x}),$$

parameterized by the coefficients $\mathbf{y} = [y_1, \ldots, y_N]^T \in \mathbb{R}^N$. Given the parameterization (3.60) we employ Tikhonov-like regularization

$$(3.61) \qquad \mathcal{R}(\widehat{q}(\cdot; \mathbf{y})) = \|\mathbf{y}\|_2^2$$

with an adaptively chosen regularization parameter μ.

In order to solve (3.40) we employ a variant of regularized Gauss-Newton method summarized in Algorithm 3.5 below. The algorithm can be applied to minimize either (3.58) or (3.48) where we let $\mathbf{X} \in \{\mathbf{T}, \mathbf{S}\}$ to denote the choice between the two. In case of noiseless data, one may simply set $r_{\mathbf{M}} = r_{\mathbf{S}} = n$.

The particular choice of Tikhonov regularization parameter (3.63) makes clear the meaning of the adaptive regularization parameter $\gamma \in (0, 1)$. Since the singular values of the Jacobian are arranged in the decreasing order, the smaller value of γ correspond to more regularization. Typically, one selects γ in the range $[0.1, 0.4]$.

4. Numerical Results. We provide here the results of numerical experiments for the following ISP setup. We consider a 2D ISP in a unit square $\Omega = [0, 1] \times [0, 1]$ with $m = 8$ extended sources placed at the top boundary $\{\mathbf{x} = [x_1, 1]^T \mid x_1 \in (0, 1)\}$, given by

$$(4.1) \qquad p_s(\mathbf{x}) = \begin{cases} 1, & \text{if} \quad \dfrac{s-1}{m} + h \leq x_1 \leq \dfrac{s}{m} - h, \\ 0, & \text{otherwise,} \end{cases} \qquad s = 1, \ldots, m,$$

where the small parameter h is defined below. The sampling wavenumbers are

$$(4.2) \qquad k_j = 15 + 5j, \quad j = 1, 2, \ldots, n,$$

Algorithm 3.5 Gauss-Newton method for solving ISP via regularized ROM mifit minimization

Input: sampling wavenumbers $0 < k_1 < k_2 < \ldots < k_n$ and the corresponding measured boundary data $\mathcal{D}^{\text{meas}}$, initial guess for potential coefficients $\mathbf{y}^{(0)} \in \mathbb{R}^N$, maximum iteration number n_{iter}, adaptive regularization parameter $\gamma \in (0,1)$.

• If $\mathbf{X} = \mathbf{S}$, use Algorithm 3.1 to compute the measured matrix $\mathbf{S}^{\text{meas}}$ from $\mathcal{D}^{\text{meas}}$; compute the eigendecomposition (3.44) and use it to find $r = r_{\mathbf{S}}$ via (3.45), the basis for the stable subspace $\mathbf{Z}_{\mathbf{S}}^r$ and the spectral projector $\mathbf{P}_{\mathbf{S}}^r$ as in (3.47);

• If $\mathbf{X} = \mathbf{T}$, use Algorithm 3.4 to compute the matrix $\mathbf{T}^{r,\text{meas}}$ from $\mathcal{D}^{\text{meas}}$, as well as $r = r_{\mathbf{M}}$ and the the basis for the stable subspace $\mathbf{Z}_{\mathbf{M}}^r$;

for $i = 1, 2, \ldots, n_{\text{iter}}$ **do**

1. Solve the forward problems (2.4)–(2.5) and (2.17)–(2.18) with $q = \widehat{q}\left(\cdot; \mathbf{y}^{(i-1)}\right)$, for all sampling wavenumbers to generate the corresponding boundary data $\mathcal{D}^{(i-1)}$;

2. Compute $\mathbf{M}^{(i-1)}$ and $\mathbf{S}^{(i-1)}$ from $\mathcal{D}^{(i-1)}$ using Algorithm 3.1;
   - If $\mathbf{X} = \mathbf{S}$, evaluate the residual $\mathbf{r}^{(i-1)} = \text{Triu}\big(\mathbf{P}_{\mathbf{S}}^r(\mathbf{S}^{\text{meas}} - \mathbf{S}^{(i-1)})\mathbf{P}_{\mathbf{S}}^r\big)$;
   - If $\mathbf{X} = \mathbf{T}$, compute $\widetilde{\mathbf{S}}^{r,(i-1)}$ and $\widetilde{\mathbf{d}}^{r,(i-1)}$ as in (3.56) and (3.57), respectively, and apply Algorithm 3.2 with $n = r_{\mathbf{M}}$ to compute $\mathbf{T}^{r,(i-1)}$, then evaluate the residual $\mathbf{r}^{(i-1)} = \text{Triu}(\mathbf{T}^{r,\text{meas}} - \mathbf{T}^{r,(i-1)})$;

3. Compute the Jacobian

$$(3.62) \qquad \mathbf{J}^{(i)} = \nabla_{\mathbf{y}} \mathcal{F}_{\mathbf{X}}^r \left(\widehat{q}\left(\cdot; \mathbf{y}^{(i-1)}\right)\right) \in \mathbb{C}^{mr(mr+1)/2 \times N},$$

   where $\mathbf{X} \in \{\mathbf{T}, \mathbf{S}\}$;

4. Compute the singular values $\sigma_1^{(i)} \geq \sigma_2^{(i)} \geq \ldots \geq \sigma_N^{(i)}$ of $\mathbf{J}^{(i)}$ and set Tikhonov regularization parameter to

$$(3.63) \qquad \mu^{(i)} = \left(\sigma_{\lfloor \gamma N \rfloor}^{(i)}\right)^2;$$

5. Compute the update direction

$$(3.64) \qquad \mathbf{z}^{(i)} = -\Re\left[\left(\left(\mathbf{J}^{(i)}\right)^* \mathbf{J}^{(i)} + \mu^{(i)} \mathbf{I}_N\right)^{-1} \left(\mathbf{J}^{(i)}\right)^* \mathbf{r}^{(i)}\right];$$

6. Use line search to find the step length

$$(3.65) \qquad \alpha^{(i)} = \operatorname*{argmin}_{\alpha \in [0, \alpha_{\max}]} \mathcal{F}_{\mathbf{X}}\left(\widehat{q}\left(\cdot; \mathbf{y}^{(i-1)} + \alpha \mathbf{z}^{(i)}\right)\right),$$

   where $\mathbf{X} \in \{\mathbf{T}, \mathbf{S}\}$ and we typically take $\alpha_{\max} = 3$;

7. Update the search potential parameters

$$(3.66) \qquad \mathbf{y}^{(i)} = \mathbf{y}^{(i-1)} + \alpha^{(i)} \mathbf{z}^{(i)}.$$

end for

Output: potential estimate $q_{\mathbf{X}}^{\text{est}} = \widehat{q}\left(\cdot; \mathbf{y}^{(n_{\text{iter}})}\right)$.

with $n = 8$.

The forward problems (2.4)–(2.5) and (2.17)–(2.18) are discretized with finite elements using Matlab PDE toolbox on a triangular mesh with mesh step $h = 0.03$ resulting in a mesh with $5,117$ nodes. The presence of mesh step parameter h in (4.1) guarantees that the numerical sources satisfy the non-overlapping condition (2.7).

The noiseless synthetic data $\mathcal{D}$ corresponding to the scattering potential q^{true} for the numerical experiments is generated by solving (2.4)–(2.5) and (2.17)–(2.18) numerically using the method described above. The noise model in the numerical experiments differs slightly from (3.43). Explicitly, instead of adding the noise to the noiseless data $\mathcal{D}$ to obtain $\mathcal{D}^{\text{meas}}$ via (3.43), the noise is added directly to the blocks $\mathbf{b}_{ij}$, $\mathbf{c}_j$, $\mathbf{d}_j$ and $\partial_k \mathbf{d}_j$, $i, j = 1, \ldots, n$, to obtain $\mathbf{b}_{ij}^{\text{noisy}}$, $\mathbf{c}_j^{\text{noisy}}$, $\mathbf{d}_j^{\text{noisy}}$ and $\partial_k \mathbf{d}_j^{\text{noisy}}$. The noise added to each entry of the four family of blocks comes from four independent identical normal distributions with zero means and standard deviations chosen to satisfy

$$
(4.3) \quad
\begin{aligned}
\frac{\sum_{j=1}^{n} \|\mathbf{d}_j^{\text{noisy}} - \mathbf{d}_j\|_F^2}{\sum_{j=1}^{n} \|\mathbf{d}_j\|_F^2} &= \frac{\sum_{j=1}^{n} \|\partial_k \mathbf{d}_j^{\text{noisy}} - \partial_k \mathbf{d}_j\|_F^2}{\sum_{j=1}^{n} \|\partial_k \mathbf{d}_j\|_F^2} \\[2mm]
&= \frac{\sum_{i \neq j} \|\mathbf{b}_{ij}^{\text{noisy}} - \mathbf{b}_{ij}\|_F^2 + \sum_{j=1}^{n} \|\mathbf{c}_j^{\text{noisy}} - \mathbf{c}_j\|_F^2}{\sum_{i \neq j} \|\mathbf{b}_{ij}\|_F^2 + \sum_{j=1}^{n} \|\mathbf{c}_j\|_F^2} = \varepsilon_{\text{noise}}^2,
\end{aligned}
$$

where $\varepsilon_{\text{noise}}$ is the desired noise level. For the numerical experiments below we take $\varepsilon_{\text{noise}} = 2.5 \cdot 10^{-2}$ corresponding to adding 2.5% noise. The blocks are then symmetrized or antisymmetrized, as appropriate, to satisfy (2.36), (3.14), (3.4) and (3.10). The blocks are then used to compute $\mathbf{M}^{\text{meas}}$ and $\mathbf{S}^{\text{meas}}$ using formulas (3.16)–(3.19).

When implementing the process outline above, it was discovered that due to numerical integration errors in computing boundary integrals (3.20)–(3.23), the resulting blocks of the stiffness and mass matrices assembled by Algorithm 3.1 differ from those obtained by (numerical) integration in (2.30)–(2.31) even in the absence of noise. This introduces a systematic error in ROM construction that can be alleviated via error estimation Algorithm 4.1 presented below.

For the numerical experiments described here it is sufficient to execute Algorithm 4.1 for $q_0 = 0$ to get accurate enough error estimates (4.4). Once the estimates are obtained, they can be used to correct the mass and stiffness matrices generated by Algorithm 3.1 by subtracting $\mathbf{E_S}$ and $\mathbf{E_M}$, respectively.

To assess the performance of the proposed approach for numerical solution of the ISP we apply both variants of Algorithm 3.5 to estimate the potential q^{2inc} that contains two inclusions, a slanted weaker extended scatterer and a localized circular scatterer of higher contrast. The potential q^{2inc} is displayed in the top left plot in Figure 1.

Algorithm 4.1 Boundary integration error estimation

Input: reference medium q_0.
- Solve the forward problems (2.4)–(2.5) and (2.17)–(2.18) numerically for the potential q_0 to generate the corresponding boundary data $\mathcal{D}_0$ and snapshots $u_{0,j}^{(s)}$, $\partial_k u_{0,j}^{(s)}$, $j = 1, \ldots, n$, $s = 1, \ldots, m$.
- Use numerical integration on the boundary $\partial\Omega$ to compute the blocks (3.20)–(3.23) and assemble the corresponding matrices $\mathbf{S}_0^{\mathcal{D}}$ and $\mathbf{M}_0^{\mathcal{D}}$ via (3.16)–(3.19).
- Use numerical integration in the bulk of Ω to compute the blocks (2.30)–(2.31) and assemble the corresponding matrices $\mathbf{S}_0^{\Omega}$ and $\mathbf{M}_0^{\Omega}$.
- Estimate the boundary integration error for stiffness and mass matrices with

$$(4.4) \qquad\qquad \mathbf{E_S} = \mathbf{S}_0^{\mathcal{D}} - \mathbf{S}_0^{\Omega}, \text{ and } \mathbf{E_M} = \mathbf{M}_0^{\mathcal{D}} - \mathbf{M}_0^{\Omega},$$

respectively.
Output: error estimate matrices $\mathbf{E_S}$ and $\mathbf{E_M}$.

To compare the performance of Algorithm 3.5 to the existing methods we implement a conventional full waveform inversion (FWI) process based on the misfit functional

$$(4.5) \qquad \mathcal{F}_{\mathrm{FWI}}(\widehat{q}) = \sum_{j=1}^{n} \left(\left\| \mathbf{d}_j^{\mathrm{meas}} - \mathbf{d}_j[\widehat{q}] \right\|_F^2 + \left\| \partial_k \mathbf{d}_j^{\mathrm{meas}} - \partial_k \mathbf{d}_j[\widehat{q}] \right\|_F^2 \right),$$

where the blocks $\mathbf{d}_j^{\mathrm{meas}}$ and $\partial_k \mathbf{d}_j^{\mathrm{meas}}$ are computed by Algorithm 3.1 from the measured data $\mathcal{D}^{\mathrm{meas}}$, while $\mathbf{d}_j[\widehat{q}]$ and $\partial_k \mathbf{d}_j[\widehat{q}]$ are computed from $\mathcal{D}[\widehat{q}]$ corresponding to the search potential $\widehat{q}$ using the same algorithm. We apply a regularized Gauss-Newton iteration to (4.5) that is essentially Algorithm 3.5 with $\mathcal{F}_{\mathbf{X}}^r$ replaced with $\mathcal{F}_{\mathrm{FWI}}$.

We perform three numerical experiments to compute the estimates of the potential $q^{2\mathrm{inc}}$. First, for the **S**-variant of Algorithm 3.5 we use noisy data with $\varepsilon_{\mathrm{noise}} = 2.5 \cdot 10^{-2}$ to compute the estimate denoted by $q_{\mathbf{S}}^{\mathrm{est}}$. Second, for the **T**-variant of Algorithm 3.5 we compute estimate $q_{\mathbf{T}}^{\mathrm{est}}$ from noiseless data. Third, for the conventional FWI with misfit (4.5) we compute the estimate $q_{\mathrm{FWI}}^{\mathrm{est}}$ from the noisy data with $\varepsilon_{\mathrm{noise}} = 2.5 \cdot 10^{-2}$. For all three experiments we set $\gamma = 0.2$. We perform $n_{\mathrm{iter}} = 10$ iterations for the first and third experiments, while taking $n_{\mathrm{iter}} = 20$ for the second. The search space $\mathcal{Q}$ is taken to contain $N = 20 \times 20 = 400$ Gaussian basis functions with peaks located on a uniform 20×20 rectangular grid in Ω.

We display in Figure 1 the estimated potentials $q_{\mathbf{S}}^{\mathrm{est}}$, $q_{\mathbf{T}}^{\mathrm{est}}$ and $q_{\mathrm{FWI}}^{\mathrm{est}}$. We observe first that $q_{\mathbf{S}}^{\mathrm{est}}$ provides the best estimate of the potential. It captures very well positions, shapes and magnitudes of both scatterers while having negligibly small artifacts even though noisy data is used. The estimate $q_{\mathbf{T}}^{\mathrm{est}}$ delivers the second best reconstruction capturing well both the locations and magnitudes of both scatterers, but introducing some artifacts in the estimate and somewhat distorting the shape of the circular scatterer. The FWI estimate $q_{\mathrm{FWI}}^{\mathrm{est}}$ recovers the topmost scatterer well, but does a poor job with the circular one missing its contrast and also splitting into two scatterers, possibly due to the effect of multiple reflections.

In order to provide quality control of potential estimates, we show in Figure 2 vertical slices of both the target potential $q^{2\mathrm{inc}}$ and all three estimates at three different locations shown
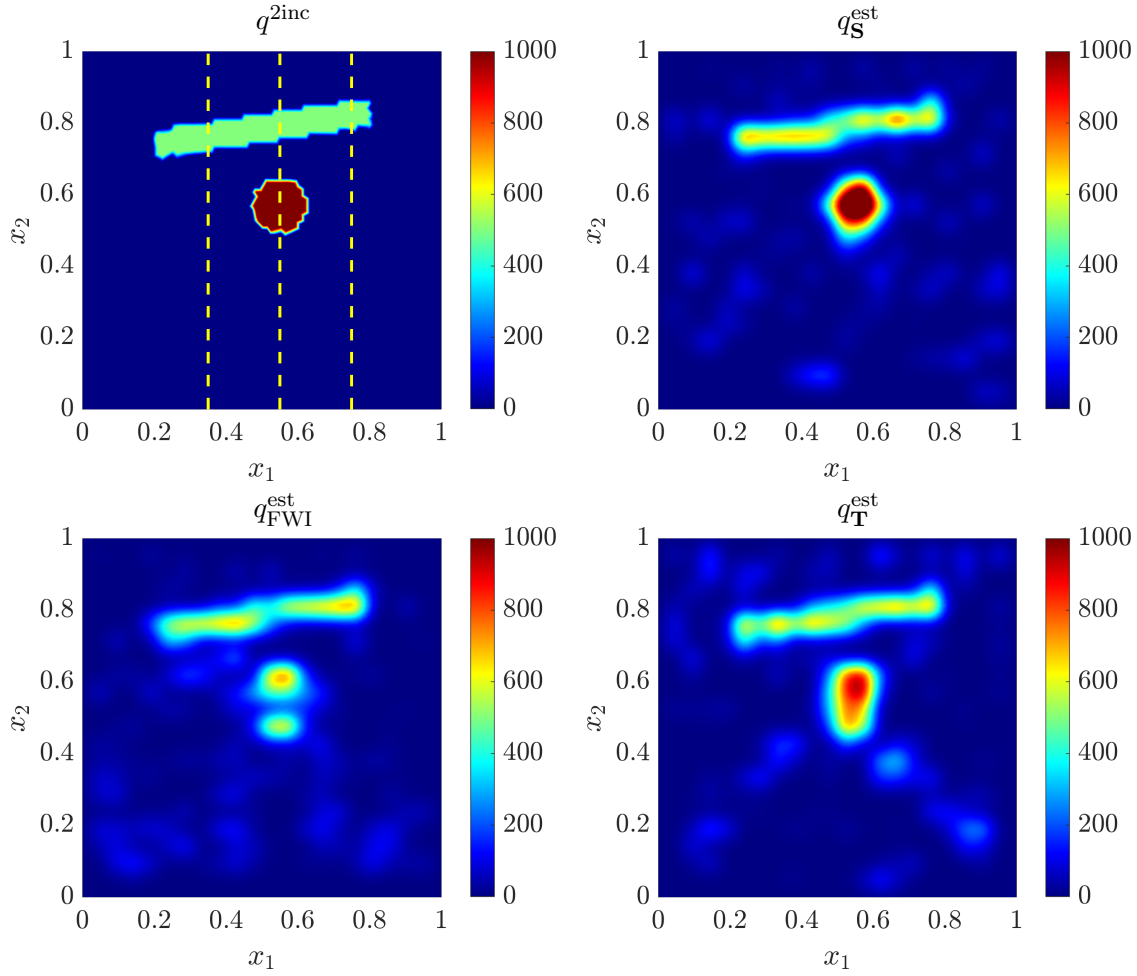
Figure 1: Model used for testing Algorithm 3.5 (top row) and estimated potentials (bottom row). The dashed yellow lines in top left plot indicate the location of vertical slices shown in quality control plots in Figure 2.

in the top left plot in Figure 1 as dashed yellow lines. Confirming our conclusions above, the vertical slices show an excellent agreement between $q^{2\mathrm{inc}}$ and $q_{\mathbf{S}}^{\mathrm{est}}$ while emphasizing some deficiencies of $q_{\mathbf{T}}^{\mathrm{est}}$ and $q_{\mathrm{FWI}}^{\mathrm{est}}$. In particular, the middle leftmost and rightmost plots shows the artifacts affecting $q_{\mathbf{T}}^{\mathrm{est}}$, while the bottom middle plot points to the poor recovery of the circular scatterer in $q_{\mathrm{FWI}}^{\mathrm{est}}$.

Overall, the **S**-variant of Algorithm 3.5 provides the best estimate $q_{\mathbf{S}}^{\mathrm{est}}$. This leads to a question of why should the **T**-variant be considered if it provides somewhat worse results numerically. This aspect is discussed in the next section.

5. Conclusions and future work. We successfully extended the approaches of [23, 24] for solving numerically the inverse scattering problem for the scattering potential of Schrödinger
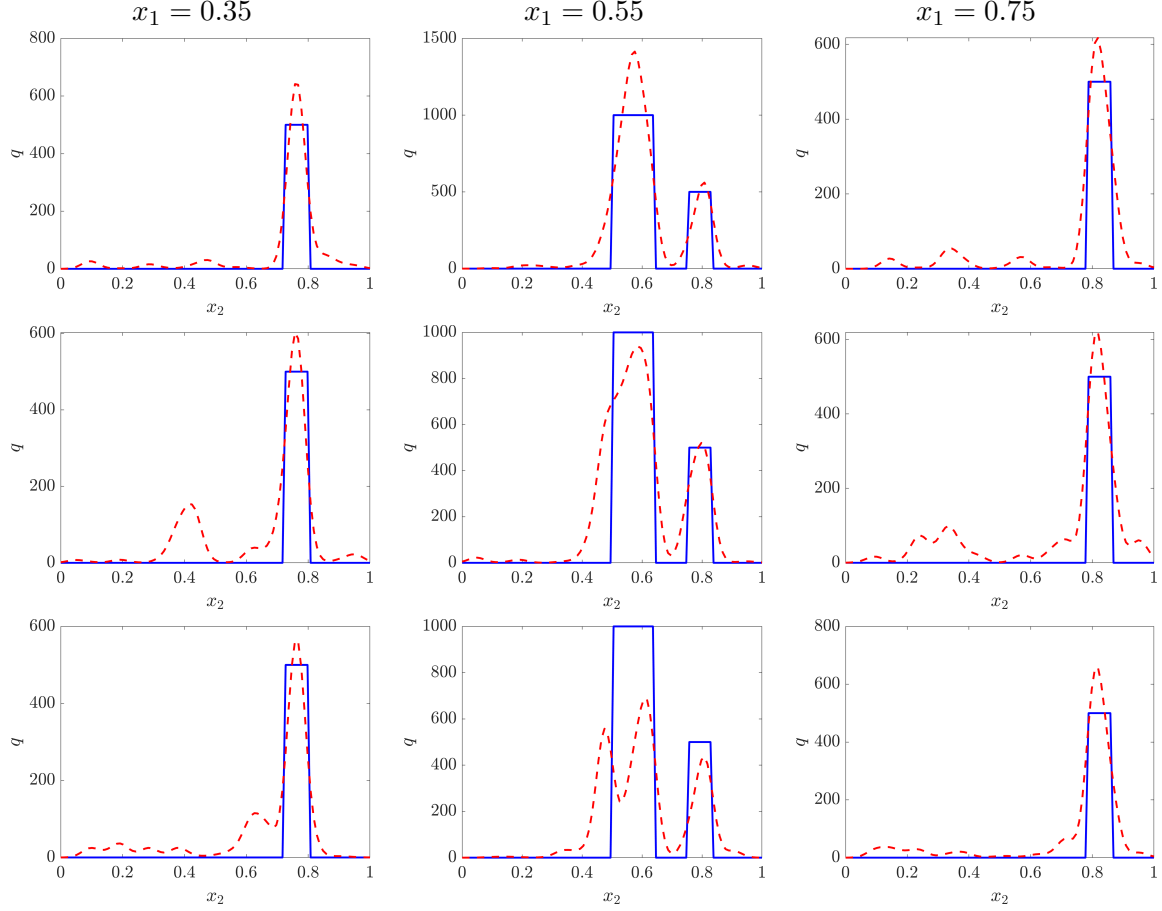
Figure 2: Potential estimate quality control: vertical slices of the target potential $q^{2\mathrm{inc}}$ (solid blue lines) and its estimates (dashed red lines) for three different values of x_1. Top row: $q_{\mathbf{S}}^{\mathrm{est}}$; middle row: $q_{\mathbf{T}}^{\mathrm{est}}$; bottom row: $q_{\mathrm{FWI}}^{\mathrm{est}}$.

using data-driven ROM to the cases of two and more spatial dimensions. We obtained the expressions for computing the mass and stiffness matrices of Schrödinger problem in Galerkin framework from the knowledge of frequency domain data measured on the boundary of the domain of interest. Algorithm 3.5 for estimating the scattering potential was developed, implemented and tested numerically displaying a potential for high quality estimates that outperform the conventional frequency domain FWI both in terms of contrast and spatial accuracy. Algorithm 3.5 admits two variants ($\mathbf{S}$ and $\mathbf{T}$) depending on which ROM matrix is fitted during the optimization process. While the numerical studies in Section 4 suggest the advantage of the $\mathbf{S}$-variant, we believe that having two variants of Algorithm 3.5 is beneficial for future research, as discussed below.

The obvious and important next step in ROM-based inversion for coefficients of wave PDEs in the frequency domain is the extension of the techniques presented here from Schrödinger

equation to Helmholtz equation. The main difference between the two is that the presence of inclusions in the medium has both the kinematic effect (changes in travel times) and scatters the probing waves in the Helmholtz case, while the kinematics in the Schrödinger case is fixed, i.e., the speed of propagation is constant. This leads to various kinds of complications for estimating the coefficient of the Helmholtz equation, including the effects like cycle-skipping that lead to severe non-convexity of conventional optimization formulations like (3.39) or (4.5). The studies of time-domain ROM-based inversion in [3, 5, 11, 12] suggest that in the presence of kinematic effects, the **T**-variant of a method similar to Algorithm 3.5, i.e., minimization of an objective like (3.58), should have an advantage over minimizing (3.48). Studying this question as well as adapting the techniques presented here to the Helmholtz case remains our immediate research priority.

Appendix A. Proofs.

Proof of Proposition 3.4. From the weak form (2.9) with $k = k_i$ we obtain

$$(A.1) \qquad \int_\Omega \overline{\nabla u_i^{(r)}} \cdot \nabla v \, d\mathbf{x} + \int_\Omega \overline{q u_i^{(r)}} v d\mathbf{x} - k_i^2 \int_\Omega \overline{u_i^{(r)}} v d\mathbf{x} + \imath k_i \int_{\partial\Omega} \overline{u_i^{(r)}} v d\Sigma = \int_{\partial\Omega} \overline{p_r} v d\Sigma,$$

for $r = 1, \ldots, m$. Taking $v = u_j^{(s)}$, $s = 1, \ldots, m$, as a test function for $i \neq j$, we use (2.30)–(2.31), (3.8) and (3.12) to get

$$(A.2) \qquad [\mathbf{s}_{ij}]_{rs} - k_i^2 [\mathbf{m}_{ij}]_{rs} + \imath k_i [\mathbf{b}_{ij}]_{rs} = [\mathbf{d}_j]_{rs}.$$

Similarly, for $k = k_j$ we have

$$(A.3) \qquad [\mathbf{s}_{ji}]_{sr} - k_j^2 [\mathbf{m}_{ji}]_{sr} + \imath k_j [\mathbf{b}_{ji}]_{sr} = [\mathbf{d}_i]_{sr}.$$

Taking the complex conjugate of (A.3) and using (2.36) gives

$$(A.4) \qquad [\mathbf{s}_{ij}]_{rs} - k_j^2 [\mathbf{m}_{ij}]_{rs} - \imath k_j [\mathbf{b}_{ij}]_{rs} = \overline{[\mathbf{d}_i]}_{sr}.$$

Subtracting (A.4) from (A.2) we obtain

$$(A.5) \qquad -k_i^2 [\mathbf{m}_{ij}]_{rs} + k_j^2 [\mathbf{m}_{ij}]_{rs} + \imath k_i [\mathbf{b}_{ij}]_{rs} + \imath k_j [\mathbf{b}_{ij}]_{rs} = [\mathbf{d}_j]_{rs} - \overline{[\mathbf{d}_i]}_{sr},$$

implying

$$(A.6) \qquad (k_j^2 - k_i^2)[\mathbf{m}_{ij}]_{rs} + \imath(k_i + k_j)[\mathbf{b}_{ij}]_{rs} = [\mathbf{d}_j]_{rs} - \overline{[\mathbf{d}_i]}_{sr}.$$

Therefore,

$$(A.7) \qquad [\mathbf{m}_{ij}]_{rs} = \frac{\overline{[\mathbf{d}_i]}_{sr} - [\mathbf{d}_j]_{rs}}{k_i^2 - k_j^2} - \imath \frac{[\mathbf{b}_{ij}]_{rs}}{k_j - k_i}, \quad r, s = 1, ..., m, \quad i \neq j.$$

Since the matrices $\mathbf{d}_i$ are complex-symmetric according to Propositon 3.1, we have

$$(A.8) \qquad \overline{[\mathbf{d}_i]}_{sr} = \overline{[\mathbf{d}_i]}_{rs}, \quad r, s = 1, \ldots, m,$$

hence

$$\overline{\mathbf{d}_i} = \overline{\mathbf{d}_i}^T = \mathbf{d}_i^*, \quad i = 1, \dots, n. \tag{A.9}$$

Thus, (A.7) becomes

$$\mathbf{m}_{ij} = \frac{\mathbf{d}_i^* - \mathbf{d}_j}{k_i^2 - k_j^2} - \imath \frac{\mathbf{b}_{ij}}{k_j - k_i}, \quad i \neq j. \tag{A.10}$$

$\blacksquare$

Proof of Proposition 3.5. For the diagonal blocks of the mass matrix we first write

$$\mathbf{m}_{ii} = \lim_{k_j \to k_i} \frac{\mathbf{m}_{ij} + \mathbf{m}_{ji}}{2}. \tag{A.11}$$

We also split the blocks of the mass matrix into $\mathbf{m}_{ij} = \mathbf{m}_{ij}^{(1)} + \mathbf{m}_{ij}^{(2)}$, where

$$\mathbf{m}_{ij}^{(1)} = \frac{\mathbf{d}_i^* - \mathbf{d}_j}{k_i^2 - k_j^2}, \tag{A.12}$$

and

$$\mathbf{m}_{ij}^{(2)} = -\imath \frac{\mathbf{b}_{ij}}{k_j - k_i}. \tag{A.13}$$

To take the limit (A.11) we first consider the contribution of (A.12). Using (A.9), we write

$$\left[\mathbf{m}_{ij}^{(1)}\right]_{rs} + \left[\mathbf{m}_{ji}^{(1)}\right]_{rs} = \frac{\overline{[\mathbf{d}_i]}_{rs} - [\mathbf{d}_j]_{rs}}{k_i^2 - k_j^2} + \frac{\overline{[\mathbf{d}_j]}_{rs} - [\mathbf{d}_i]_{rs}}{k_j^2 - k_i^2} \tag{A.14}$$

$$= \frac{[\mathbf{d}_j]_{rs} - \overline{[\mathbf{d}_i]}_{rs} + \overline{[\mathbf{d}_j]}_{rs} - [\mathbf{d}_i]_{rs}}{k_j^2 - k_i^2} \tag{A.15}$$

$$= \frac{1}{k_j + k_i} \frac{[\mathbf{d}_j]_{rs} - [\mathbf{d}_i]_{rs} + \overline{[\mathbf{d}_j]}_{rs} - \overline{[\mathbf{d}_i]}_{rs}}{k_j - k_i}. \tag{A.16}$$

As $k_j \to k_i$, we observe that

$$2\mathbf{m}_{ii}^{(1)} = \frac{1}{2k_i}\left(\partial_k \mathbf{d}_i + \overline{\partial_k \mathbf{d}_i}\right) = \frac{1}{k_i}\Re(\partial_k \mathbf{d}_i), \quad i = 1, \dots, n. \tag{A.17}$$

For the contribution of (A.13) we have

$$\left[\mathbf{m}_{ij}^{(2)}\right]_{rs} + \left[\mathbf{m}_{ji}^{(2)}\right]_{rs} = -\imath \frac{[\mathbf{b}_{ij}]_{rs}}{k_j - k_i} - \imath \frac{[\mathbf{b}_{ji}]_{rs}}{k_i - k_j}. \tag{A.18}$$

Since $[\mathbf{b}_{ij}]_{rs} = \int_{\partial\Omega} \overline{u^r(\mathbf{x}; k_i)} u^s(\mathbf{x}; k_j) d\Sigma$, we write

$$-\left[\mathbf{m}_{ij}^{(2)}\right]_{rs} - \left[\mathbf{m}_{ji}^{(2)}\right]_{rs} = \frac{\imath}{k_j - k_i}\int_{\partial\Omega} \overline{u^r(\mathbf{x}; k_i)} u^s(\mathbf{x}; k_j) d\Sigma + \frac{\imath}{k_i - k_j}\int_{\partial\Omega} \overline{u^r(\mathbf{x}; k_j)} u^s(\mathbf{x}; k_i) d\Sigma =$$

$$= \frac{\imath}{k_j - k_i}\int_{\partial\Omega} \left(\overline{u^r(\mathbf{x}; k_i)}\{u^s(\mathbf{x}; k_j) - u^s(\mathbf{x}; k_i)\} - u^s(\mathbf{x}; k_i)\{\overline{u^r(\mathbf{x}; k_j)} - \overline{u^r(\mathbf{x}; k_i)}\}\right) d\Sigma.$$

As $k_j \to k_i$, we obtain

$$(A.19) \quad -\lim_{j \to i}\left(\left[\mathbf{m}_{ij}^{(2)}\right]_{rs} + \left[\mathbf{m}_{ji}^{(2)}\right]_{rs}\right) = \imath \int_{\partial\Omega}\left(\overline{u^r(\mathbf{x};k_i)}\partial_k u^s(\mathbf{x};k_i) - u^s(\mathbf{x};k_i)\overline{\partial_k u^r(\mathbf{x};k_i)}\right)d\Sigma,$$

hence

$$(A.20) \qquad 2\left[\mathbf{m}_{ii}^{(2)}\right]_{rs} = \imath \int_{\partial\Omega}\left(-\overline{u^r(\mathbf{x};k_i)}\partial_k u^s(\mathbf{x};k_i) + u^s(k_i,x)\overline{\partial_k u^r(\mathbf{x};k_i)}\right)d\Sigma,$$

which gives

$$(A.21) \qquad\qquad 2\mathbf{m}_{ii}^{(2)} = \imath\mathbf{c}_i, \quad i = 1,\ldots,n.$$

Combining (A.17) and (A.21), we obtain that

$$(A.22) \qquad\qquad \mathbf{m}_{ii} = \frac{1}{2k_i}\Re\left(\partial_k \mathbf{d}_i\right) + \frac{\imath}{2}\mathbf{c}_i, \quad i = 1,\ldots,n. \qquad\qquad \blacksquare$$

Proof of Proposition 3.2. We recall from (A.2) for $i \neq j$ that

$$(A.23) \qquad\qquad [\mathbf{s}_{ij}]_{rs} - k_i^2[\mathbf{m}_{ij}]_{rs} + \imath k_i[\mathbf{b}_{ij}]_{rs} = [\mathbf{d}_j]_{rs},$$

which we multiply by k_j^2 to obtain

$$(A.24) \qquad\qquad k_j^2[\mathbf{s}_{ij}]_{rs} - k_j^2 k_i^2[\mathbf{m}_{ij}]_{rs} + \imath k_j^2 k_i[\mathbf{b}_{ij}]_{rs} = k_j^2[\mathbf{d}_j]_{rs}.$$

Similarly,

$$(A.25) \qquad\qquad k_i^2[\mathbf{s}_{ij}]_{rs} - k_i^2 k_j^2[\mathbf{m}_{ij}]_{rs} - \imath k_i^2 k_j[\mathbf{b}_{ij}]_{rs} = k_i^2\overline{[\mathbf{d}_i]}_{sr}.$$

Subtracting (A.25) from (A.24) we have

$$(A.26) \qquad k_j^2[\mathbf{s}_{ij}]_{rs} - k_i^2[\mathbf{s}_{ij}]_{rs} + \imath k_j^2 k_i[\mathbf{b}_{ij}]_{rs} + \imath k_i^2 k_j[\mathbf{b}_{ij}]_{rs} = k_j^2[\mathbf{d}_j]_{rs} - k_i^2\overline{[\mathbf{d}_i]}_{sr},$$

implying

$$(A.27) \qquad [\mathbf{s}_{ij}]_{rs} = \frac{k_j^2[\mathbf{d}_j]_{rs} - k_i^2\overline{[\mathbf{d}_i]}_{sr}}{k_j^2 - k_i^2} - \frac{\imath k_j^2 k_i[\mathbf{b}_{ij}]_{rs} + \imath k_i^2 k_j[\mathbf{b}_{ij}]_{rs}}{k_j^2 - k_i^2}$$

$$(A.28) \qquad\qquad = \frac{k_i^2\overline{[\mathbf{d}_i]}_{sr} - k_j^2[\mathbf{d}_j]_{rs}}{k_i^2 - k_j^2} - \imath\frac{k_j^2 k_i + k_i^2 k_j}{k_j^2 - k_i^2}[\mathbf{b}_{ij}]_{rs}, \quad r,s = 1,\ldots,m,\ i \neq j.$$

Using (A.9) yields the desired result. $\qquad\qquad\blacksquare$

Proof of Proposition 3.3. Introducing $\mathbf{f}_j = k_j^2\mathbf{d}_j$, $j = 1,\ldots,n$, the entries of the stiffness matrix blocks can be written as

$$(A.29) \qquad [\mathbf{s}_{ij}]_{rs} = \frac{\overline{[\mathbf{f}_i]}_{rs} - [\mathbf{f}_j]_{rs}}{k_i^2 - k_j^2} - \imath\frac{k_j^2 k_i + k_i^2 k_j}{k_i + k_j}\frac{[\mathbf{b}_{ij}]_{rs}}{k_i - k_j}, \quad r,s = 1,\ldots,m,$$

for $i \neq j$. Similarly to the proof of Proposition 3.5, we can obtain that

$$
\begin{aligned}
2[\mathbf{s}_{ii}]_{rs} = & \frac{1}{k_i} \Big([\partial_k \mathbf{f}_i]_{rs} + \overline{[\partial_k \mathbf{f}_i]}_{rs} \Big) + \\
& \frac{\imath 2 k_i^3}{2 k_i} \int_{\partial \Omega} \Big(- \overline{u^r(\mathbf{x}; k_i)} \partial_k u^s(\mathbf{x}; k_i) + u^s(\mathbf{x}; k_i) \overline{\partial_k u^r(\mathbf{x}; k_i)} \Big) d\Sigma,
\end{aligned}
\tag{A.30}
$$

hence

$$
\begin{aligned}
2[\mathbf{s}_{ii}]_{rs} = & \frac{1}{2 k_i} \Big(k_i^2 [\partial_k \mathbf{d}_i]_{rs} + k_i^2 [\mathbf{d}_i]_{rs} + k_i^2 \overline{[\partial_k \mathbf{d}_i]}_{sr} + k_i^2 \overline{[\mathbf{d}_i]}_{sr} \Big) + \\
& \imath k_i^2 \int_{\partial \Omega} \Big(- \overline{u^r(\mathbf{x}; k_i)} \partial_k u^s(\mathbf{x}; k_i) + u^s(\mathbf{x}; k_i) \overline{\partial_k u^r(\mathbf{x}; k_i)} \Big) d\Sigma,
\end{aligned}
\tag{A.31}
$$

for $i = 1, \ldots, n$. Simplifying and using the definition (3.13) we find

$$
\mathbf{s}_{ii} = \frac{1}{2} \Big(k_i \Re(\partial_k \mathbf{d}_i) + 2 \Re(\mathbf{d}_i) \Big) + \frac{\imath k_i^2}{2} \mathbf{c}_i, \quad i = 1, \ldots, n. \quad \blacksquare
\tag{A.32}
$$

Appendix B. Proof of Theorem 2.3. Before proving the desired result, we recall the following variant of the implicit function theorem, see, e.g., [10, 16].

Theorem B.1. Consider $F : \mathbb{R} \times H \to W$, where H and W are Banach spaces. Assume that there exists an open set $I \subset \mathbb{R}$ such that for every $k \in I$ there exists a unique $u = u(k) \in H$ such that

$$
F(k, u) = 0.
\tag{B.1}
$$

Then if

$$
F : \mathbb{R} \times H \to W
\tag{B.2}
$$

is continuous, and

$$
\partial_u F : \mathbb{R} \times H \to W
\tag{B.3}
$$

is continuous, and

$$
\forall k \in I : \ (\partial_u F(k, u))^{-1} : W \to H
\tag{B.4}
$$

exists and is bounded, then there exists a continuous map such that

$$
I \ni k \mapsto u(k) \in H.
\tag{B.5}
$$

Also, if $\partial_k F$ is continuous, we obtain that u is Frechét-differentiable and its derivative at k_0 is given by

$$
[\partial_k u](k_0) = - \{ \partial_u F(k_0, u(k_0)) \}^{-1} \partial_k F(k_0, u(k_0)).
\tag{B.6}
$$

To prove Theorem 2.3 we take

(B.7) $$F^{(s)} : (k, u) \in \mathbb{R}_+ \times H^1(\Omega) \to H^1(\Omega)', \quad s = 1, \ldots, m,$$

defined by (2.15). Observe that for every open interval $I \subset \mathbb{R}_+$, relation (B.1) holds by the well posedness of the forward problem. Thus, we have

(B.8) $$\partial_u F^{(s)}\left(k_0, u^{(s)}(k_0)\right) = \mathcal{S} - k_0^2 \mathcal{M} + \imath k_0 \mathcal{B}$$

and

(B.9) $$\partial_k F^{(s)}\left(k_0, u^{(s)}(k_0)\right) = (-2k_0 \mathcal{M} + \imath \mathcal{B})u^{(s)}(k_0).$$

Plugging (B.8) and (B.9) into (B.6), we get

(B.10) $$\left[\partial_k u^{(s)}\right](k_0) = \left(\mathcal{S} - k_0^2 \mathcal{M} + \imath k_0 \mathcal{B}\right)^{-1} \left(2k_0 \mathcal{M} u^{(s)}(k_0) + \imath \mathcal{B} u^{(s)}(k_0)\right).$$

Thus, in order to compute $w^{(s)} = \partial_k u^{(s)}(k_0)$ one has to solve (2.17) with boundary condition (2.18).

Appendix C. Proof sketch of Theorem 2.1. Here we sketch the proof of Theorem 2.1. We follow a setting similar to that in [26, 23]. For that reason we study the complex conjugate version of (2.9), that is to find $u^{(s)} \in H^1(\Omega)$ such that for any $v \in H^1(\Omega)$ it satisfies

(C.1) $$\int_\Omega \nabla u^{(s)} \cdot \overline{\nabla v}\, d\mathbf{x} + \int_\Omega q u^{(s)} \overline{v} d\mathbf{x} - k^2 \int_\Omega u^{(s)} \overline{v} d\mathbf{x} - \imath k \int_{\partial\Omega} u^{(s)} \overline{v} d\Sigma = \int_{\partial\Omega} p_s \overline{v} d\Sigma.$$

We begin by defining the forms $a_1, a_2 : H^1(\Omega)^2 \to \mathbb{C}$ as

(C.2) $$a_1(u, v) = \int_\Omega \nabla u \cdot \overline{\nabla v} d\mathbf{x} - \imath k \int_{\partial\Omega} u \overline{v} d\Sigma,$$

(C.3) $$a_2(u, v) = -\int_\Omega u \overline{v} d\mathbf{x} + \frac{1}{k^2} \int_\Omega q u \overline{v} d\mathbf{x},$$

for $u, v \in H^1(\Omega)$. We note that a_1 is coercive and bounded, while a_2 is bounded.

Let us define the linear Riesz isomorphism

(C.4) $$\Phi : H^1(\Omega) \to \overline{H^1(\Omega)}',$$

as $\Phi u = \langle u, \cdot \rangle_{\overline{H^1(\Omega)}'}$ for $u \in H^1(\Omega)$, and with $\overline{H^1(\Omega)}'$ denoting the antidual of the space $H^1(\Omega)$. Since $a_1(u, \cdot)$ is an antilinear functional on $H^1(\Omega)$, and using the Lax-Milgram lemma, we define $\mathcal{T} : H^1(\Omega) \to H^1(\Omega)$ as

(C.5) $$a_1(u, v) = \langle \mathcal{T} u, v \rangle_{\overline{H^1(\Omega)}'},$$

with $\mathcal{T}$ being one-to-one and onto.

We also define the linear operator $\mathcal{W} : L^2(\Omega) \to \overline{H^1(\Omega)}'$, $u \overset{\mathcal{W}}{\mapsto} a_2(u, \cdot)$, and two linear maps

$$(C.6) \qquad \mathcal{A}_1 = \mathcal{T}^{-1}\Phi^{-1}\mathcal{W} : L^2(\Omega) \to H^1(\Omega),$$

$$(C.7) \qquad \mathcal{A} = \mathcal{A}_1 \circ id_{H^1(\Omega) \to L^2(\Omega)} : H^1(\Omega) \overset{c}{\hookrightarrow} L^2(\Omega) \to H^1(\Omega), \quad s \mapsto \mathcal{A}_1 s,$$

where $id_{H^1(\Omega) \to L^2(\Omega)}$ is the compact embedding operator of $H^1(\Omega)$ into $L^2(\Omega)$. Also, for $v \in H^1(\Omega)$ and $w \in H^1(\Omega)$, we have $a_1(\mathcal{A}v, w) = a_2(v, w)$. We claim that $\mathcal{I} + k^2\mathcal{A}$ is one-to-one.

Finding a solution of (C.1) is equivalent to finding $u^{(s)} \in H^1(\Omega)$ such that for all $v \in H^1(\Omega)$ it satisfies

$$(C.8) \qquad a_1(u^{(s)}, v) + k^2 a_2(u^{(s)}, v) = \langle P^{(s)}, v\rangle_{\overline{H^1(\Omega)}'} \iff$$

$$(C.9) \qquad a_1(u^{(s)}, v) + k^2 a_1(\mathcal{A}u^{(s)}, v) = \langle P^{(s)}, v\rangle_{\overline{H^1(\Omega)}'} \iff$$

$$(C.10) \qquad a_1(u^{(s)} + k^2 \mathcal{A}u^{(s)}, v) = \langle P^{(s)}, v\rangle_{\overline{H^1(\Omega)}'} \iff$$

$$(C.11) \qquad \left\langle \mathcal{T}\left(u^{(s)} + k^2\mathcal{A}u^{(s)}\right), v\right\rangle_{\overline{H^1(\Omega)}'} = \langle P^{(s)}, v\rangle_{\overline{H^1(\Omega)}'},$$

hence

$$(C.12) \qquad \Phi\mathcal{T}(\mathcal{I} + k^2\mathcal{A})u^{(s)} \overset{\overline{H^1(\Omega)}'}{=} P^{(s)} \iff$$

$$(C.13) \qquad (\mathcal{I} + k^2\mathcal{A})u^{(s)} = \mathcal{T}^{-1}\Phi^{-1}P^{(s)} \in H^1(\Omega).$$

Since $\mathcal{A} \in \mathcal{L}(H^1(\Omega), H^1(\Omega))$ is compact and $\mathcal{I} + k^2\mathcal{A}$ is injective, using the Fredholm alternative we obtain that there exists a unique element $u^{(s)} \in H^1(\Omega)$ that satisfies (C.13). We also obtain the forward stability estimate

$$\|u^{(s)}\|_{H^1(\Omega)} \leq \|(\mathcal{I} + k^2\mathcal{A})^{-1}\|_{\mathcal{L}(H^1(\Omega), H^1(\Omega))}\|\mathcal{T}^{-1}\|_{\mathcal{L}(H^1(\Omega), H^1(\Omega))}$$
$$\|\Phi^{-1}\|_{\mathcal{L}(H^1(\Omega), \overline{H^1(\Omega)}')}\|P^{(s)}\|_{\overline{H^1(\Omega)}'}.$$

The above argument establishes that for all $v \in H^1(\Omega)$, a unique weak solution of (C.1) exists. Therefore, by taking the complex conjugate of (C.1), we conclude that there exists a unique solution of (2.9).

REFERENCES

[1] L. Borcea, V. Druskin, A. Mamonov, S. Moskow, and M. Zaslavsky, *Reduced order models for spectral domain inversion: embedding into the continuous problem and generation of internal data*, Inverse Problems, 36 (2020), p. 055010.
[2] L. Borcea, V. Druskin, A. V. Mamonov, and M. Zaslavsky, *A model reduction approach to numerical inversion for a parabolic partial differential equation*, Inverse Problems, 30 (2014), p. 125011.
[3] L. Borcea, V. Druskin, A. V. Mamonov, M. Zaslavsky, and J. Zimmerling, *Reduced order model approach to inverse scattering*, SIAM Journal on Imaging Sciences, 13 (2020), pp. 685–723.
[4] L. Borcea, J. Garnier, A. V. Mamonov, and J. Zimmerling, *Reduced order model approach for imaging with waves*, Inverse Problems, 38 (2021), p. 025004.
[5] L. Borcea, J. Garnier, A. V. Mamonov, and J. Zimmerling, *Waveform inversion via reduced order modeling*, Geophysics, 88 (2023), pp. R175–R191.

[6] L. Borcea, J. Garnier, A. V. Mamonov, and J. Zimmerling, *Waveform inversion with a data driven estimate of the internal wave*, SIAM Journal on Imaging Sciences, 16 (2023), pp. 280–312.

[7] L. Borcea, J. Garnier, A. V. Mamonov, and J. Zimmerling, *When data driven reduced order modeling meets full waveform inversion*, SIAM Review, 66 (2024), pp. 501–532.

[8] M. Cheney, *Inverse scattering in dimension two*, Journal of Mathematical Physics, 25 (1984), pp. 94–107.

[9] S. Coen, M. Cheney, and A. Weglein, *Velocity and density of a two-dimensional acoustic medium from point source surface data*, Journal of Mathematical Physics, 25 (1984), pp. 1857–1861.

[10] T. J. Connolly and D. J. N. Wall, *On frechet differentiability of some nonlinear operators occurring in inverse problems: an implicit function theorem approach*, Inverse Problems, 6 (1990), p. 949.

[11] V. Druskin, A. V. Mamonov, A. E. Thaler, and M. Zaslavsky, *Direct, nonlinear inversion algorithm for hyperbolic problems via projection-based model reduction*, SIAM Journal on Imaging Sciences, 9 (2016), pp. 684–747.

[12] V. Druskin, A. V. Mamonov, and M. Zaslavsky, *A nonlinear method for imaging with acoustic waves via reduced order model backprojection*, SIAM Journal on Imaging Sciences, 11 (2018), pp. 164–196.

[13] V. Druskin, S. Moskow, and M. Zaslavsky, *Lippmann–schwinger–lanczos algorithm for inverse scattering problems*, Inverse Problems, 37 (2021), p. 075003.

[14] V. Druskin, S. Moskow, and M. Zaslavsky, *On extension of the data driven rom inverse scattering framework to partially nonreciprocal arrays*, Inverse Problems, 38 (2022), p. 084002.

[15] B. Engquist and A. Majda, *Absorbing boundary conditions for numerical simulation of waves*, Proceedings of the National Academy of Sciences, 74 (1977), pp. 1765–1766.

[16] M. Hinze, R. Pinnau, M. Ulbrich, and S. Ulbrich, *Optimization with PDE Constraints*, Mathematical Modelling: Theory and Applications, Springer Netherlands, 2008.

[17] D. Li and J. M. Harris, *Full waveform inversion with nonlocal similarity and model-derivative domain adaptive sparsity-promoting regularization*, Geophysical Journal International, 215 (2018), pp. 1841–1864.

[18] Y. Maday, A. T. Patera, and G. Turinici, *A priori convergence theory for reduced-basis approximations of single-parameter elliptic partial differential equations*, Journal of Scientific Computing, 17 (2002), pp. 437–446.

[19] A. V. Mamonov, L. Borcea, J. Garnier, and J. Zimmerling, *Velocity estimation via model order reduction*, in SEG International Exposition and Annual Meeting, SEG, 2022, p. D011S040R003.

[20] R. Newton, *Inverse scattering. II. Three dimensions*, Journal of Mathematical Physics, 21 (1980), pp. 1698–1715.

[21] R. Newton, *Inverse Schrödinger Scattering in Three Dimensions*, Texts and monographs in physics, Springer-Verlag, 1989.

[22] A. Pladys, R. Brossier, Y. Li, and L. Métivier, *On cycle-skipping and misfit function modification for full-wave inversion: Comparison of five recent approaches*, GEOPHYSICS, 86 (2021), pp. R563–R587.

[23] A. Tataris and T. van Leeuwen, *Reduced order model based nonlinear waveform inversion for the 1d helmholtz equation*, Acta Applicandae Mathematicae, 194 (2024), p. 11.

[24] T. van Leeuwen and A. Tataris, *A data-driven approach to solving a 1D inverse scattering problem*, AIP Advances, 13 (2023). 065310.

[25] K. Veroy, C. Prud'Homme, D. Rovas, and A. Patera, *A posteriori error bounds for reduced-basis approximation of parametrized noncoercive and nonlinear elliptic partial differential equations*, in 16th AIAA Computational Fluid Dynamics Conference, 2003, p. 3847.

[26] A. Wald and T. Schuster, *Tomographic Terahertz Imaging Using Sequential Subspace Optimization*, Springer International Publishing, Cham, 2018, pp. 261–290.